CrossMark

ORIGINAL PAPER

Effect of pristine and functionalized single- and multi-walled carbon nanotubes on CO_2 separation of mixed matrix membranes based on polymers of intrinsic microporosity (PIM-1): a molecular dynamics simulation study

Karim Golzar[1] · Hamid Modarress[1] · Sepideh Amjad-Iranagh[1]

Abstract Molecular dynamics (MD) and grand canonical Monte Carlo (GCMC) simulations were conducted to investigate the transport properties of carbon dioxide, methane, nitrogen, and oxygen through pure and mixed matrix membranes (MMMs) based on polymers of intrinsic microporosity (PIM-1). For this purpose, first, 0.5 to 3 wt% of pristine single-walled carbon nanotube (p-SWCNT) and multi-walled carbon nanotube (p-MWCNT) were embedded into the pure PIM-1, and then for better dispersion of CNT particles into the polymer matrix and to improve the performance of the resulting MMMs, polyethylene glycol (PEG) functionalized SWCNT and MWCNT (f-SWCNT and f-MWCNT, respectively) were loaded. The characterization of the obtained MMMs was carried out by using density, glass transition temperature, X-ray pattern, and fractional free volume calculations. Comparing the obtained results with the available reported experimental data, indicate the authenticity of the applied simulation approach. The simulation results exhibit that the pristine and PEG-functionalized CNT particles improve the transport properties such as diffusivity, solubility, and permeability of the PIM-1 membranes, without sacrificing their selectivity. Also, the MMMs incorporated with 2 wt% of the functionalized CNT particles indicate better performance for the CO_2 separation from other gases. According to the calculated results, the highest permeability and diffusivity for CO_2 are observed in the [PIM-1/f-SWCNT] MMM among the other membranes which represent that the loading of the f-SWCNTs can enhance the CO_2 separation performance of PIM-1 more than other CNTs studied in this work.

Introduction

It is known that carbon dioxide (CO_2) is not only the main greenhouse gas but also an important potential carbon source, therefore, the capture and separation of CO_2 has attracted worldwide attention [1, 2]. Compared with other methods used for CO_2 separation, such as absorption (including chemical and physical absorption) [3, 4], adsorption [5, 6] and cryogenic separation [7], membrane separation is more attractive owing to low cost, low energy consumption, and high flexibility [8–10].

The two types of membranes which are generally used in gas separation include polymeric and inorganic membranes [11, 12]. The polymeric membranes have the following advantages: favorable mechanical flexibility, simple processing ability, and economical cost productivity as well as having effective separation properties such as diffusivity, solubility, and permeability for various gas mixtures [7]. However, despite these advantages and progresses, the performance of pure polymeric membranes is generally restricted by the trade-off limitation between gas permeability and selectivity which is the so-called Robeson upper bound [13, 14]. To overcome this limitation, some modifications on polymers are usually needed. In recent years, mixed matrix membranes

✉ Hamid Modarress
hmodares@aut.ac.ir

[1] Department of Chemical Engineering, Amirkabir University of Technology, Tehran, Iran

(MMMs) which are synergistic combination of organic polymers with inorganic nanofillers (permeable, as well as impermeable) were suggested [5, 15]. In MMMs, nanofillers are dispersed into the polymeric matrix and as a result by incorporating the desirable mechanical and processing properties of polymeric matrix with useful molecular sieving properties of inorganic nanofiller, the trade-off problem of pure polymeric membranes in gas separation process will be resolved [16, 17]. Since the permeability of polymeric membranes is mainly related to the chain mobility and the fractional free volume of the polymer structure, the loading of rigid nanofillers with particle size close to the characteristic size of the macromolecules, by hindering molecular chain packing and increasing free volume, improves the gas permeability of the produced selective nanocomposite polymeric membranes [6, 18].

In the development of MMMs, the appropriate material selection for both the polymer matrix and the nanofiller as an inorganic disperse phase is important. A novel type of polymers with relatively high gas permeability and moderate selectivity was described as polybenzodioxanes by McKeown et al. [19] and McKeown and Maksheed [20] for the first time. These polymers which were termed polymers of intrinsic microporosity (PIMs) are a class of high fractional free volume (~0.20), large apparent surface area (~800 m^2/g), glassy (the glass transition temperature is higher than 400 °C) and ladder type polymers with very rigid and contorted backbone [4, 21–23]. Among the PIMs, the most interesting member of this class is PIM-1 which is synthesized by the polycondensation reaction of 5,5,6,6-tetrahydroxy–3,3,3,3-tetramethyl–1,1′-spirobisindane with tetra-fluorophathalonitrile (see Fig. 1) [24]. PIM-1, due to containing the contorted angled spirobisindane unit, is able to optimize permeability and selectivity by changing the polymer chain packing, and also has the relative ease of synthesizing the high molecular weight of PIM-1 while having suitable thermal and chemical stabilities [4, 21, 25–28]; in this work, the PIM-1 was selected as matrix in studied membranes.

Some different fillers such as zeolites [29], carbon molecular sieves [30], metal organic frameworks [31], activated carbons [32], silica [21], and carbon nanotubes (CNTs) [5, 33–37] have been extensively used in MMMs fabrication. In comparison to the other fillers, CNTs due to their outstanding properties including superior gas separation, inherent smoothness, hydrophobic graphitic walls, extremely high aspect

ratios, and mechanical properties have been most proposed as the best candidate fillers for gas separation in MMMs [5, 12, 13, 38, 39]. CNTs with tubular structure and nanoscale diameter were observed by Iijima for the first time, and were synthesized by rolling up cylinders of graphite sheets as singular tubes or several concentric graphitic shells which were called single-walled carbon nanotubes (SWCNTs) and multi-walled carbon nanotubes (MWCNTs), respectively [9, 12, 17, 40–45]. When CNTs are embedded into the polymers, due to inherent smoothness of CNTs and changing the chain packing of the resulting MMMs in effect of polymer chains-CNT particles interactions, the permeability is significantly enhanced by increasing diffusivity [28, 36, 46]. Therefore, in this work, among several inorganic nanofillers, the CNTs were chosen as an inorganic disperse phase into the PIM-1 matrix.

On the other hand, to achieve the more appropriate gas transport properties in [polymer/CNT] MMMs, the CNT particles should be smoothly distributed into the polymeric matrix [13, 15]. For this purpose and to enhance the CNT adhesion to the polymer chain, some functionalization methods such as grafting chemical agents (surface oxidation groups, hydrophilic groups, polar groups, etc.) to the surface of the CNT particles and non-covalent surface coating with surfactants and polymer chains have been widely applied [13]. There are some advantages and disadvantages for these methods. In the functionalization method with chemical agents, the distribution of CNTs was appropriately done but structure and original properties of CNT particles may be destroyed. However, in the non-covalent functionalization method, due to relatively mild reaction conditions, the graphitic structure and pristine properties of CNTs could be maintained but their dispersion is not very smooth [40, 47]. Therefore, in this work, to facilitate CNTs dispersion into the PIM-1 matrix in uniform format and as a result increase the performance of studied MMMs, the surface of used CNTs was functionalized with poly(ethylene glycol) (PEG) as a spacer (see Fig. 2) [13].

In this work, five distinguished types (17 samples) of PIM-1 (hereafter abbreviated to PIM) membranes were simulated by Materials Studio 6.0 (MS) software [48]. All the simulated membranes had PIM as their matrix but the type and the amounts of the added CNT particles to their matrix were different. In the first type of membranes, pure PIM was used without adding CNT particles as the nanofillers. In the second
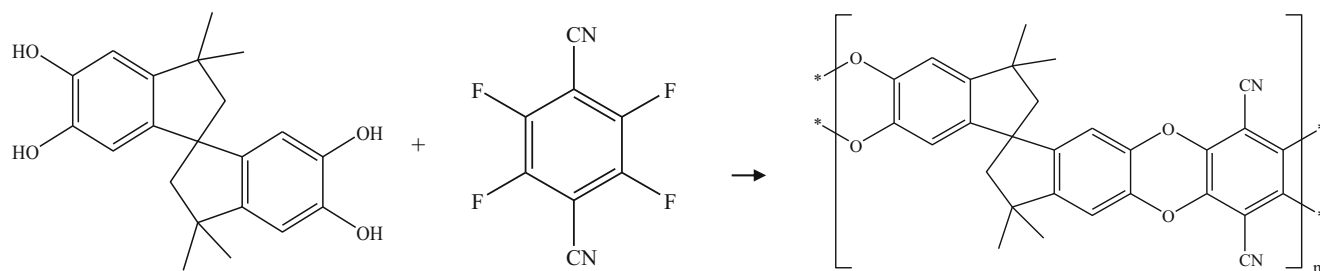
Fig. 1 The chemical reaction for preparing the pure PIM-1
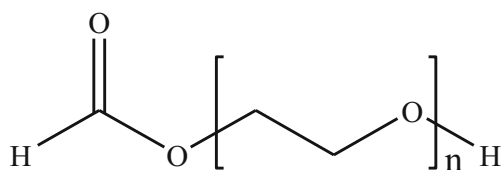
Fig. 2 The chemical structure of PEG repeating unit

type of membranes, the pristine single-walled carbon nano-tubes (*p*-SWCNTs) were added as the nanofillers to the PIM matrix to obtain the MMMs which were abbreviated as [PIM/*p*-SWCNT] MMMs. In the third type of membranes, the PEG-functionalized single-walled carbon nanotubes (*f*-SWCNTs) were added as the nanofillers to the PIM matrix to obtain [PIM/*f*-SWCNT] MMMs. In the fourth type of membranes, the pristine multi-walled carbon nanotubes (*p*-MWCNTs) were added as the nanofillers to the PIM matrix to obtain [PIM/*p*-MWCNT] MMMs. In the fifth type of membranes, the PEG-functionalized multi-walled carbon nanotubes (*f*-MWCNTs) were added to PIM matrix to obtain [PIM/*f*-MWCNT] MMMs. In all the MMMs the amounts of pristine and functionalized CNT particles (SWCNT and MWCNT) were 0.5 to 3 wt%. The abbreviations used to refer to the simulated membranes are presented in Table 1. To characterize the simulated membranes, the physical properties of the membranes including density, glass transition temperature, X-ray diffraction pattern, and fractional free volume were calculated. In addition, the transport properties of CO_2, CH_4, N_2, and O_2 through these membranes which included the diffusivity, solubility, and permeability of each gas, as well as, the membrane selectivity for their binary mixtures (CO_2/CH_4), (CO_2/N_2), (CO_2/O_2), (CH_4/N_2), (CH_4/O_2), and (N_2/O_2) were evaluated. Several experimental [1–3, 8, 9, 11, 12, 21, 23, 40, 49] and simulation [18, 41, 50–54] studies investigated the relationship between structure and properties of pure and mixed matrix membranes. However, our literature research indicates that there is not an experimental or simulation work which has fully understood the physical and transport properties of pure PIM and its mixed matrix membranes which were filled by pristine and chemically functionalized SWCNT and MWCNT particles. So, the structure–properties relationships of these membranes as well as their mechanism of gas separation are yet unknown. Therefore, the main goal of this work is to achieve detailed information about physical and gas transport properties of pure and mixed matrix membranes based on PIM and CNT particles by using molecular dynamics (MD) and grand canonical Monte Carlo (GCMC) simulations.

Methods

The initialization in the MD simulation consists of two major stages, constructing the polymeric membranes in the simulation

Table 1 The list of abbreviations for the simulated pure PIM membrane and its MMMs with their matrix, CNT types, and wt% of CNTs

| Abbreviation	Membrane		
	Matrix	CNT type	wt% of CNT
Pure PIM		(−)[a]	(−)[a]
[PIM/*p*-SWCNT(0.5%)] MMM		*p*-SWCNT	0.5
[PIM/*p*-SWCNT(1%)] MMM			1
[PIM/*p*-SWCNT(2%)] MMM			2
[PIM/*p*-SWCNT(3%)] MMM			3
[PIM/*f*-SWCNT(0.5%)] MMM		*f*-SWCNT	0.5
[PIM/*f*-SWCNT(1%)] MMM			1
[PIM/*f*-SWCNT(2%)] MMM			2
[PIM/*f*-SWCNT(3%)] MMM	PIM-1		3
[PIM/*p*-MWCNT(0.5%)] MMM		*p*-MWCNT	0.5
[PIM/*p*-MWCNT(1%)] MMM			1
[PIM/*p*-MWCNT(2%)] MMM			2
[PIM/*p*-MWCNT(3%)] MMM			3
[PIM/*f*-MWCNT(0.5%)] MMM		*f*-MWCNT	0.5
[PIM/*f*-MWCNT(1%)] MMM			1
[PIM/*f*-MWCNT(2%)] MMM			2
[PIM/*f*-MWCNT(3%)] MMM			3

[a] without CNTs

cells and choosing the appropriate force field for calculating the interactions between atoms in the simulation cells.

Constructing the polymeric membranes

All the MD simulations were carried out by using MS software. The monomers of PIM and PEG were built by 'Homopolymer Builder Module' of this software [18, 50, 51]. The initial configurations of the repeating units (as shown in Fig. 3(a and c)) and randomly generated polymeric chains, with 100 repeating unites for PIM and three for PEG (as shown in Fig. 3(b and d)) were constructed by using "Homopolymer Builder Module' of the MS software. This module is only capable of creating polymer chains with single backbone whereas PIM is a ladder polymer and has two backbones. Therefore, to construct the ladder PIM chain, the procedure of Heuchel et al. [24] was applied. The geometry optimization and energy minimization of the initial polymer chain structures were performed by using the 'Forcite Module' and the 'Smart Minimizer' function of 'Discover Module' of MS software [18, 50, 51, 53]. In the minimization procedure, to accelerate the computational procedure in an appropriate simulation time, the steepest-descent method was consecutively switched to the conjugated gradient and then to the Newton methods to reduce the required energy derivatives and to eliminate all the close contacts to obtain accurate results in 20,000 steps [50, 55–57].

Fig. 3 The initial molecular configurations of repeating units for: (a) PIM and (c) PEG; the initial randomly generated polymeric chain configurations with 100 degree of polymerization for (b) PIM and 3 degree of polymerization for (d) PEG; (e) molecular configurations of *p*-SWCNT; (f) molecular configurations of *f*-SWCNT; (g) molecular configurations of *p*-MWCNT, and (h) molecular configurations of *f*-MWCNT. The atoms in repeating units, polymeric chains and CNT configurations are shown by color balls: C (gray), H (white), N (blue), and O (red)
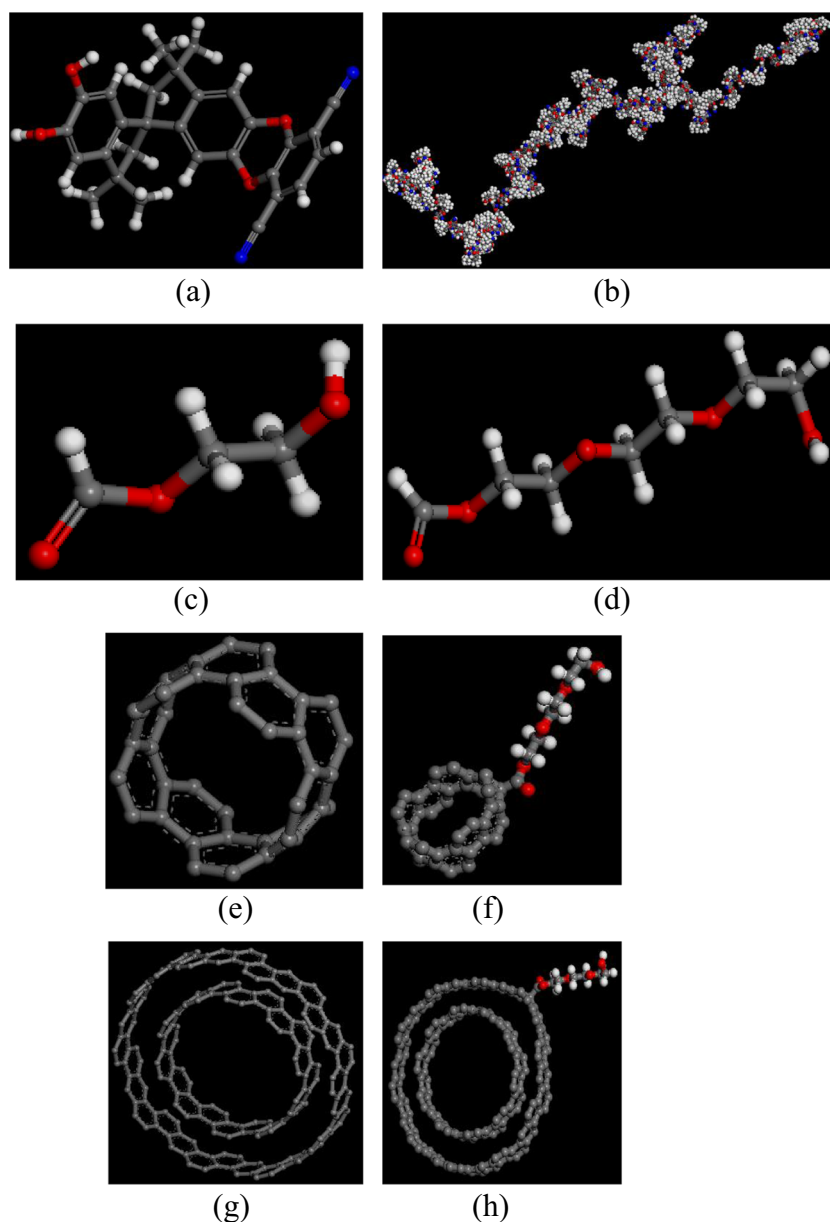
The structures of SWCNT and MWCNT in pristine form with same length (4.92 Å) and different diameters (6.78 Å for SWCNT and 13.56 Å for MWCNT) were constructed using 'Nanostructure Builder Module' of MS software [18, 50, 51, 55]. Then, a single 3-mer PEG chain was grafted to the pristine SWCNT and MWCNT to build PEG-functionalized SWCNT and MWCNT and on the resulting structures the geometry optimization and energy minimization, as described above, were performed. The final molecular configurations of *p*-SWCNT, *f*-SWCNT, *p*-MWCNT, and *f*-MWCNT are represented respectively in Fig. 3(e, f, g, and h).

To construct amorphous cells containing pure PIM and its MMMs, the following procedure was conducted. At the first stage, a predetermined number of polymer chains and CNT particles (as presented in Table 2) were embedded in the simulation cell by applying the periodic boundary conditions (*pbc*) [18, 50, 51, 55] and by using the 'Amorphous Cell Module' of the MS software [18, 29]. The number of polymer chains and CNT particles were changed so that the weight percent of CNT particles in the MMMs, expressed as ([CNT/(PIM + CNT)]%), matched with the experimental values [58]. The initial density of these cells was set to 0.1 (g/cm³). This allowed the systems to fluctuate continuously in the course of simulation [18, 49–52, 57, 59] and finally attain the real cell configuration by matching the density with the experimental value (as reported in Table 3). After this stage, the initially generated amorphous *pbc* cells were subjected to energy minimization for 20,000 iterations to achieve relaxation. Then, on the relaxed amorphous cells containing pure PIM or its MMMs, *NPT* (constant number of atoms in the

Table 2 The number of polymer chains for PIM and PEG and CNT particles in simulated pure PIM membrane and its MMMs along with weight percent of CNT particles in each membrane

Membranes	Number of polymer chains and CNTs						[CNT/(CNT + PIM)]%
	PIM	PEG	p-SWCNT	f-SWCNT	p-MWCNT	f-MWCNT	
Pure PIM	4	0	0	0	0	0	0.00
[PIM/p-SWCNT(0.5%)] MMM	4	0	2	0	0	0	0.51
[PIM/p-SWCNT(1%)] MMM	4	0	4	0	0	0	1.02
[PIM/p-SWCNT(2%)] MMM	4	0	8	0	0	0	2.03
[PIM/p-SWCNT(3%)] MMM	4	0	12	0	0	0	3.01
[PIM/f-SWCNT(0.5%)] MMM	6	3	0	3	0	0	0.51
[PIM/f-SWCNT(1%)] MMM	6	6	0	6	0	0	1.01
[PIM/f-SWCNT(2%)] MMM	6	12	0	12	0	0	1.98
[PIM/f-SWCNT(3%)] MMM	6	19	0	19	0	0	3.06
[PIM/p-MWCNT(0.5%)] MMM	10	0	0	0	1	0	0.51
[PIM/p-MWCNT(1%)] MMM	10	0	0	0	2	0	1.02
[PIM/p-MWCNT(2%)] MMM	10	0	0	0	4	0	2.03
[PIM/p-MWCNT(3%)] MMM	10	0	0	0	6	0	3.01
[PIM/f-MWCNT(0.5%)] MMM	12	1	0	0	0	1	0.47
[PIM/f-MWCNT(1%)] MMM	12	2	0	0	0	2	0.95
[PIM/f-MWCNT(2%)] MMM	12	5	0	0	0	5	2.09
[PIM/f-MWCNT(3%)] MMM	12	7	0	0	0	7	2.98

simulation cell, at 2 bar pressure and 30 °C temperature) MD simulations for a period of 5 ns were performed using 'Discover Module' of MS software [49, 52] at a time step of 1 fs, to eliminate the local stresses and to obtain the equilibrated simulation cells with realistic density and with the lowest potential energy [18, 50, 57] (as shown in Table 4).

To achieve further relaxation of the simulation cells, the residual internal energy of the constructed membranes was removed by applying the annealing process [50, 59]. This process was performed by using the temperature cycle protocol in the 'Forcite Module' of MS software [52, 57] where each simulation cell was heated at 40 °C intervals from 200 to 600 °C. It should

Table 3 The simulation results and the available experimental data for density (g/cm³) of the simulated pure PIM membrane and its MMMs by using the force fields

Membranes	PCFF	DERIDING	COMPASS
Pure PIM	1.124 (1.117[a])	1.325	1.231
[PIM/p-SWCNT(0.5%)] MMM	1.128	1.330	1.235
[PIM/p-SWCNT(1%)] MMM	1.132	1.334	1.239
[PIM/p-SWCNT(2%)] MMM	1.140	1.343	1.248
[PIM/p-SWCNT(3%)] MMM	1.147	1.352	1.256
[PIM/f-SWCNT(0.5%)] MMM	1.127	1.328	1.234
[PIM/f-SWCNT(1%)] MMM	1.130	1.332	1.237
[PIM/f-SWCNT(2%)] MMM	1.135	1.338	1.243
[PIM/f-SWCNT(3%)] MMM	1.141	1.345	1.250
[PIM/p-MWCNT(0.5%)] MMM	1.129	1.331	1.236
[PIM/p-MWCNT(1%)] MMM	1.134	1.337	1.242
[PIM/p-MWCNT(2%)] MMM	1.144	1.348	1.252
[PIM/p-MWCNT(3%)] MMM	1.153	1.360	1.263
[PIM/f-MWCNT(0.5%)] MMM	1.129	1.330	1.236
[PIM/f-MWCNT(1%)] MMM	1.133	1.336	1.241
[PIM/f-MWCNT(2%)] MMM	1.142	1.346	1.251
[PIM/f-MWCNT(3%)] MMM	1.151	1.357	1.261

[a] is the experimental value from [60]

Table 4 The evaluated potential energies (average ± standard deviation) in 10^6 kcal mol^{-1} for the simulated pure PIM membrane and its MMMs by using the force fields

Membranes	PCFF	DERIDING	COMPASS
Pure PIM	−5.54 ± 0.06	−9.54 ± 0.23	−8.46 ± 0.18
[PIM/p-SWCNT(0.5%)] MMM	−4.24 ± 0.05	−7.30 ± 0.12	−6.47 ± 0.24
[PIM/p-SWCNT(1%)] MMM	−4.11 ± 0.11	−7.08 ± 0.15	−6.28 ± 0.35
[PIM/p-SWCNT(2%)] MMM	−3.87 ± 0.04	−6.66 ± 0.08	−5.91 ± 0.14
[PIM/p-SWCNT(3%)] MMM	−3.02 ± 0.06	−5.20 ± 0.12	−4.61 ± 0.43
[PIM/f-SWCNT(0.5%)] MMM	−4.18 ± 0.09	−7.20 ± 0.16	−6.38 ± 0.26
[PIM/f-SWCNT(1%)] MMM	−3.97 ± 0.12	−6.84 ± 0.19	−6.06 ± 0.15
[PIM/f-SWCNT(2%)] MMM	−3.56 ± 0.07	−6.13 ± 0.34	−5.44 ± 0.09
[PIM/f-SWCNT(3%)] MMM	−2.95 ± 0.11	−5.08 ± 0.47	−4.50 ± 0.36
[PIM/p-MWCNT(0.5%)] MMM	−2.56 ± 0.14	−4.41 ± 0.15	−3.91 ± 0.16
[PIM/p-MWCNT(1%)] MMM	−2.31 ± 0.06	−3.98 ± 0.54	−3.53 ± 0.33
[PIM/p-MWCNT(2%)] MMM	−2.01 ± 0.04	−3.46 ± 0.18	−3.07 ± 0.27
[PIM/p-MWCNT(3%)] MMM	−1.93 ± 0.08	−3.32 ± 0.23	−2.95 ± 0.53
[PIM/f-MWCNT(0.5%)] MMM	−1.54 ± 0.11	−2.65 ± 0.42	−2.35 ± 0.42
[PIM/f-MWCNT(1%)] MMM	−1.23 ± 0.15	−2.12 ± 0.12	−1.88 ± 0.17
[PIM/f-MWCNT(2%)] MMM	−1.11 ± 0.10	−1.91 ± 0.33	−1.70 ± 0.29
[PIM/f-MWCNT(3%)] MMM	−1.02 ± 0.09	−1.76 ± 0.55	−1.56 ± 0.13

be noted that, the higher temperature (600 °C) was set well above the glass transition temperature (T_g) of the studied polymeric membranes (T_g ~430 °C). Then the simulation cells were cooled down to the initial temperature (200 °C) at the intervals of 40 °C, where at each temperature, 1000 ps *NPT* MD simulations were performed. After this stage, an additional 5 ns *NVT* (constant number of atoms in the simulation cell, volume, and temperature at 30 °C) MD simulation was performed to achieve the final equilibrium molecular structures of the studied membranes corresponding to the experimentally reported physical properties such as density [50], glass transition temperature [18], X-ray diffraction pattern [29, 57], and fractional free volume [59]. At this stage of the MD simulation the atomic trajectories were saved every 1000 ps to be used in subsequent analysis and examination of the membrane properties.

The force filed

In atomistic simulation study of multi-particle systems, the appropriate force field should be capable of calculating the important interactions accurately, and thereby reduces the simulation time [18, 59]. The force fields which are commonly used in the MD simulations are: condensed-phase optimized molecular potential for atomistic simulation studies (COMPASS) force field [18, 41, 55, 57], polymer-consistent force field (PCFF) [24], and DREIDING force field [61, 62]. Preliminary investigations in the initialization stage of this work, in accord with previous reports [24], indicated that the PCFF force field is the most appropriate force field, since in this force field the rotational angles in the repeating units of the studied PIMs are properly parameterized and therefore, by its application accurate values

for a number of physical properties such as density and potential energy with minimum fluctuations can be obtained. The simulated results for the density of the studied polymeric membranes by application of above mentioned force fields, compared with the available experimental data, are presented in Table 3, which indicates that the PCFF force field is the most suitable for these MD simulations. This point is also confirmed by considering the reported results in Table 4, where lower calculated potential energies with smaller fluctuations have been obtained by application of this force field.

In this work, by using PCFF force field, the electrostatic and van der Waals interactions were respectively evaluated by the Ewald summation method (with the accuracy of 0.001 kcal mol^{-1} [57]) and by the Lennard–Jones 6–12 function [63]. The values of Lenard-Jones interaction (ε/κ_B) and size (σ) parameters along with the critical temperature (T_c) of the studied gases (CO_2, CH_4, N_2, and O_2) are presented in Table 5.

The equations of motion were integrated by the velocity Verlet algorithm [18, 51] with a time step of 1 fs. To proceed with the simulation procedure in a reasonable time and obtain accurate results, the cut-off distance to calculate the non-bond interactions was taken as less than half of the simulation cell length [18, 51]. The simulation cell lengths along with cut-off distances with a spline width of 0.1 Å and a buffer width of 0.05 Å [39] for all the simulated membranes are reported in Table 6.

The thermostat and barostat

To select the best thermostat and barostat for regulating temperature (at 30 °C) and pressure (at 2 bar) during *NPT* and

Table 5 Critical temperature (T_c), Lenard-Jones interaction (ε/κ_B), and size (σ) parameters of CO_2, CH_4, N_2, and O_2 gases [50, 52]

Gas	T_c (K)	ε/κ_B (K)	σ (Å)
CO_2	304.2	213.4	3.5
CH_4	190.7	154.7	3.8
N_2	126.2	83.0	3.6
O_2	154.4	112.7	3.4

NVT MD simulation procedures, three thermostats (Nose-Hoover [39], Berendson [41], and Anderson [29]) and three barostats (Anderson [56], Berendson [18], and Parrinello [39]) were examined. Table 7 shows the evaluated average regulating temperature and pressure with their standard deviations by using various thermostats and barostats. It is seen in Table 7 that the Nose-Hoover thermostat (with a Q ratio of 0.005 and relaxation time of 0.1 ps [18, 39, 50, 51]) and also, the Anderson barostat (with a decay of 0.5 ps [14]) are more accurate than the others. Therefore, they were used throughout the *NPT* and *NVT* MD simulations to regulate the temperature and pressure.

Results and discussion

Equilibrium validation

The attainment of the equilibrium in the constructed simulation cells can be validated by using *NPT* ensemble (at 2 bar and 30 °C) for 5 ns of MD simulation and by considering the occurrence of small fluctuations in the potential energy and

Table 6 The equilibrium cell length l (Å) and the cut-off distance (Å) for the simulated pure PIM membrane and its MMMs

Membranes	l (Å)	Cut-off distance (Å)
Pure PIM	64.99	32
[PIM/p-SWCNT(0.5%)] MMM	65.03	33
[PIM/p-SWCNT(1%)] MMM	65.06	
[PIM/p-SWCNT(2%)] MMM	65.14	
[PIM/p-SWCNT(3%)] MMM	65.21	
[PIM/f-SWCNT(0.5%)] MMM	74.60	37
[PIM/f-SWCNT(1%)] MMM	74.81	
[PIM/f-SWCNT(2%)] MMM	75.21	
[PIM/f-SWCNT(3%)] MMM	75.70	
[PIM/p-MWCNT(0.5%)] MMM	88.23	44
[PIM/p-MWCNT(1%)] MMM	88.25	
[PIM/p-MWCNT(2%)] MMM	88.30	
[PIM/p-MWCNT(3%)] MMM	88.35	
[PIM/f-MWCNT(0.5%)] MMM	93.77	47
[PIM/f-MWCNT(1%)] MMM	93.81	
[PIM/f-MWCNT(2%)] MMM	94.05	
[PIM/f-MWCNT(3%)] MMM	94.12	

temperature and also obtaining densities for the simulation cells in agreement with the experimental values. Figure 1S(a, b, and c) shows three examples for the equilibrium attainment of the simulation cells for the potential energy, temperature, and density, respectively for the MMMs including [PIM/p-SWCNT(0.5%)], [PIM/f-SWCNT(0.5%)], and [PIM/p-MWCNT(0.5%)]. It is observed that both the potential energy and temperature have very small fluctuations and have been stabilized in the course of MD simulations which in turn, prove that the equilibration in all of the simulation cells has been attained. Also, as shown in Fig. 1S(c), the simulated densities approach a constant value after 2000 ps, which indicates that the simulation time adjustment at 5000 ps (5 ns) suffices for calculating the desired properties of the studied membranes.

The final molecular configurations of the simulated structure of pure PIM and its MMMs at equilibrium state are presented as snapshots in Fig. 4. As seen in Fig. 4(a), in the membrane consisting of pure PIM, the polymer chains have folded and packed together smoothly filling all space of the simulation cell. However, as shown in Fig. 4(b to q) for the [PIM/CNT] MMMs, the interactions between the polymer chains of PIM and the CNTs prevent the chain packing. Therefore, the PIM chains are separated from each other by the CNT particles located between them and distributed in the polymeric matrix of the MMMs. Also, Fig. 4(b, c, d, f, g, h, j, k, l, n, o, and p) shows a smooth distribution of pristine and functionalized CNT particles at the loading of 0.5 to 2 wt%, whereas at 3 wt% loading, the agglomeration is observed (see Fig. 4(e, i, m, and q)). Therefore, there must be a threshold for addition of CNT particles into the polymer matrix to prevent the CNT particles agglomeration which can be explained by considering the molecular interactions. That is, the stronger molecular interactions between polymer-polymer chains and CNT-CNT particles compared with those of polymer chains and CNT particles, would cause packing of polymer chains and the agglomeration of CNT particles. This seems to occur at 3 wt% CNT particles.

Also on comparing the snapshots presented for the pristine CNT particles (Fig. 4(b, c, d, e, j, k, l, and m)) with those of the functionalized ones (Fig. 4(f, g, h, i, n, o, p, and q)), it is seen that the functionalized CNT particles are distributed more smoothly among the PIM chains. This can be attributed to presence of PEG chains which act as the spacers and by the separating the CNT particles, weakening their interactions. This enables the polymer chains to drag the functionalized CNT particles inside the folded polymer chains and as a result make them more smoothly distributed into the polymeric matrix. Figure 4 shows that the occurrence of agglomeration in [PIM/p-MWCNT] and [PIM/f-MWCNT] MMMs is more severe than [PIM/p-SWCNT] and [PIM/f-SWCNT] MMMs which arises due to stronger interactions between MWCNTs (either pristine or functionalized MWCNTs) than those of the corresponding SWCNTs.

Further confirmation for the obtained final molecular configurations of the simulated membranes can be presented by

Table 7 Comparison of capability of the thermostats and barostats to regulate the temperature at 30 °C (obtained average temperature by thermostat ± standard deviation) and the pressure at 2 bar (obtained average by barostat ± standard deviation) in MD and GCMC simulations for simulated pure PIM membrane and its MMMs

Membranes	Thermostat (°C)			Barostat (bar)		
	Nose-Hoover	Berendson	Anderson	Anderson	Berendson	Parrinello
Pure PIM	29.46 ± 0.34	35.87 ± 0.76	34.76 ± 0.48	2.04 ± 0.58	2.57 ± 0.36	2.84 ± 0.37
[PIM/p-SWCNT(0.5%)] MMM	30.97 ± 0.12	36.74 ± 0.52	35.57 ± 0.45	2.06 ± 0.42	2.77 ± 0.47	2.61 ± 0.86
[PIM/p-SWCNT(1%)] MMM	31.64 ± 0.23	33.67 ± 0.47	33.56 ± 0.66	2.12 ± 0.78	2.69 ± 0.90	2.63 ± 0.43
[PIM/p-SWCNT(2%)] MMM	31.86 ± 0.25	32.68 ± 0.58	34.78 ± 0.24	2.08 ± 0.55	2.84 ± 0.87	2.70 ± 0.56
[PIM/p-SWCNT(3%)] MMM	30.67 ± 0.32	36.89 ± 0.53	35.79 ± 0.67	2.07 ± 0.35	2.84 ± 0.45	2.70 ± 0.84
[PIM/f-SWCNT(0.5%)] MMM	30.04 ± 0.58	33.57 ± 0.12	31.78 ± 0.78	2.11 ± 0.78	2.68 ± 0.34	2.88 ± 0.67
[PIM/f-SWCNT(1%)] MMM	30.57 ± 0.33	34.70 ± 0.37	34.78 ± 0.22	2.05 ± 0.32	2.72 ± 0.56	2.76 ± 0.34
[PIM/f-SWCNT(2%)] MMM	32.78 ± 0.45	38.75 ± 0.79	38.54 ± 0.34	2.08 ± 0.68	2.49 ± 0.78	2.91 ± 0.56
[PIM/f-SWCNT(3%)] MMM	31.63 ± 0.21	34.67 ± 0.53	34.80 ± 0.66	2.03 ± 0.57	2.86 ± 0.22	3.01 ± 0.88
[PIM/p-MWCNT(0.5%)] MMM	30.38 ± 0.22	36.78 ± 0.68	36.86 ± 0.88	2.15 ± 0.78	2.78 ± 0.68	2.68 ± 0.43
[PIM/p-MWCNT(1%)] MMM	31.97 ± 0.32	37.64 ± 0.32	31.57 ± 0.43	2.18 ± 0.22	2.73 ± 0.96	2.48 ± 0.45
[PIM/p-MWCNT(2%)] MMM	32.78 ± 0.35	30.64 ± 0.78	38.35 ± 0.78	2.09 ± 0.57	2.87 ± 0.43	2.51 ± 0.78
[PIM/p-MWCNT(3%)] MMM	30.55 ± 0.31	32.68 ± 0.46	33.89 ± 0.54	2.11 ± 0.46	2.51 ± 0.56	2.80 ± 0.44
[PIM/f-MWCNT(0.5%)] MMM	31.79 ± 0.36	36.89 ± 0.78	35.79 ± 0.23	2.08 ± 0.89	2.69 ± 0.86	2.92 ± 0.36
[PIM/f-MWCNT(1%)] MMM	33.45 ± 0.31	36.78 ± 0.33	32.38 ± 0.68	2.13 ± 0.32	2.49 ± 0.32	3.05 ± 0.58
[PIM/f-MWCNT(2%)] MMM	31.97 ± 0.23	34.78 ± 0.57	31.78 ± 0.79	2.09 ± 0.67	2.58 ± 0.46	2.90 ± 0.53
[PIM/f-MWCNT(3%)] MMM	30.45 ± 0.46	34.95 ± 0.36	37.57 ± 0.84	2.15 ± 0.56	2.87 ± 0.89	2.47 ± 0.57

investigating the molecular interactions between PIM chains and CNT particles. For this purpose, the radial distribution function (RDF) for molecular interaction of PIM chain and p-SWCNT, f-SWCNT, p-MWCNT, and f-MWCNT particles in [PIM/p-SWCNT(2%)], [PIM/f-SWCNT(2%)], [PIM/p-MWCNT(2%)], and [PIM/f-MWCNT(2%)] MMMs was respectively evaluated by using the 'Discover Module' of MS software [50, 54] and the results are represented in Fig. 5. As seen in Fig. 5, the intensity of RDF peaks for the molecular interaction of PIM chains with the CNT particles is in the order of: f-SWCNT > p-SWCNT > f-MWCNT > p-MWCNT, which indicates that the SWCNT particles have stronger interaction with PIM chain compared with those of MWCNT particles. Also, by functionalizing the CNT particles with PEG, these interactions will be intensified significantly. The RDF results also indicate that the SWCNT particles have higher affinity to interact with PIM chains and as a result, instead of agglomeration, they are smoothly distributed between the PIM chains. Whereas the MWCNT particles have lower affinity to interact with polymer chains and then they are partially agglomerated, as mentioned above and seen in Fig. 5. These results are consistent with those obtained by SEM study [13].

Therefore, by comparing the simulation cells as presented in Fig. 4, it can be stated that addition of pristine and functionalized CNT particles affects the chain packing of PIM matrix, and thereby changes the physical properties of the membrane such as density, glass transition temperature, X-ray pattern, and fractional free volume as well as gas transport properties including diffusivity, solubility, permeability, and selectivity.

## Physical characteristics

Glass transition temperature

The glass transition temperature (T_g) is a characteristic which indicates the chain flexibility and consequently affects the transport properties of the membranes. The procedure for calculating T_g has been explained in previous publications [18, 50, 51, 56]. Figure 6 shows the simulation results, as an example, for determination of T_g by evaluating the specific volume of [PIM/f-MWCNT(0.5%)] MMM versus temperature. It is seen from this figure that on temperature increase, the specific volume of MMM rises linearly, with an abrupt change in the slopes; 0.001 cm^3/g °C and 0.0034 cm^3/g °C respectively for the temperature ranges (200 to 400 °C) and (440 to 600 °C), where the evaluated linear correlation coefficients (R^2s) are presented in Fig. 6. Therefore, by extrapolating the linear plots, the T_g of [PIM/f-MWCNT(0.5%)] MMM was calculated at the intersection as 434.58 °C. The calculated T_gs for pure PIM and its MMMs are reported in Table 8. Since the matrix of the studied MMMs is PIM which is a ladder type glassy polymer with high free volume and with rigid backbone, it would not experience any rotational mobility in its backbone even at high temperature (> 400 °C), so it
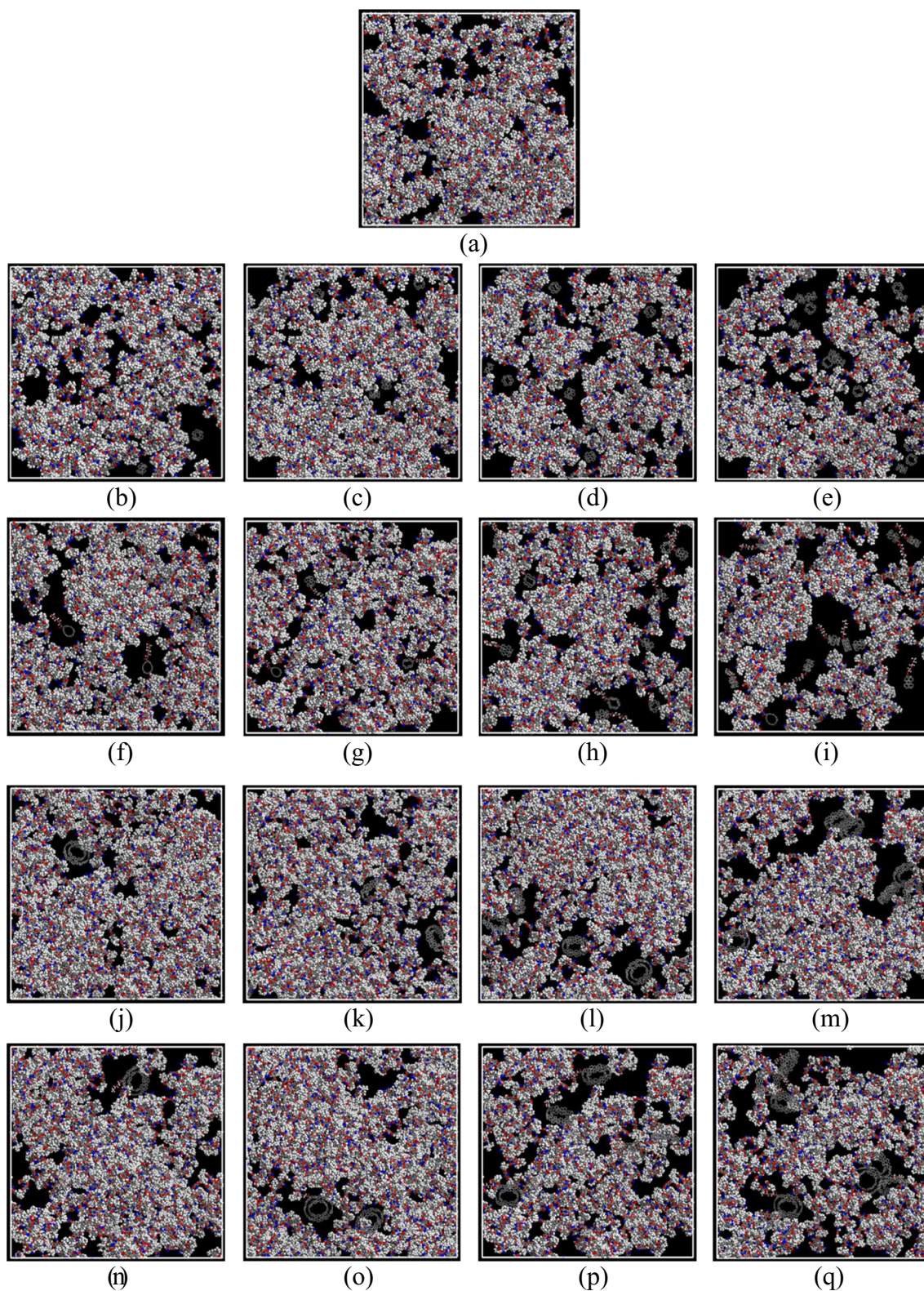
Fig. 4 The final molecular configuration of amorphous cells, after 5 ns *NVT* MD simulations at 30 °C and 2 bar for (a) Pure PIM, (b) [PIM/*p*-SWCNT(0.5%)], (c) [PIM/*p*-SWCNT(1%)], (d) [PIM/*p*-SWCNT(2%)], (e) [PIM/*p*-SWCNT(3%)], (f) [PIM/*f*-SWCNT(0.5%)], (g) [PIM/*f*-SWCNT(1%)], (h) [PIM/*f*-SWCNT(2%)], (i) [PIM/*f*-SWCNT(3%)], (j) [PIM/*p*-MWCNT(0.5%)], (k) [PIM/*p*-MWCNT(1%)], (l) [PIM/*p*-MWCNT(2%)], (m) [PIM/*p*-MWCNT(3%)], (n) [PIM/*f*-MWCNT(0.5%)], (o) [PIM/*f*-MWCNT(1%)], (p) [PIM/*f*-MWCNT(2%)] and (q) [PIM/*f*-MWCNT(3%)] MMMs. The atoms in repeating units, polymeric chains and CNT configurations are shown by color balls: C (gray), H (white), N (blue), and O (red)
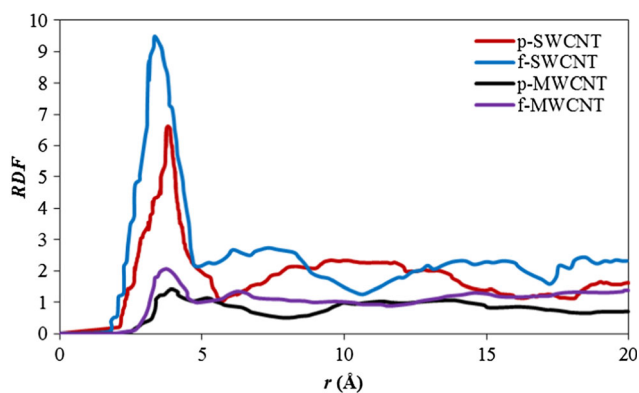
Fig. 5 The *RDF* curves for molecular interaction of PIM chains and *p*-SWCNT, *f*-SWCNT, *p*-MWCNT, and *f*-MWCNT particles in [PIM/*p*-SWCNT(2%)], [PIM/*f*-SWCNT(2%)], [PIM/*p*-MWCNT(2%)], and [PIM/*f*-MWCNT(2%)] MMMs, respectively

has been explained in several experimental studies [8, 9, 43, 44, 65], it is experimentally difficult to measure a T_g for this polymer before degradation. However, based on some experimental studies a T_g for pure PIM has been suggested to be higher than 400 °C [58, 66] and it seems to correspond with the reported T_g by [64] at 436 °C. Our simulation results on PIM as pure and MMMs indicated that on increasing the temperature above the calculated T_g (434.58 °C) up to 600 °C no degradation occurred then the evaluated T_g for pure PIM is considered in agreement with the reported experimental T_g by [64].

On the other hand, the obtained simulation results (Table 8) indicate that by adding CNT particles into the pure PIM, the T_gs of MMMs increases. This can be attributed to temperature resistance of CNT particles which in turn cause thermal stability in the PIM matrix. As seen in Table 8, on addition of *f*-SWCNT or *f*-MWCNT into the PIM matrix, the T_gs of the resulting MMMs increase compared with those of *p*-SWCNT or *p*-MWCNT. This phenomenon can be ascribed to stronger molecular interaction of functionalized CNT particles with the polymer chains in comparison to the pristine CNT particles and also, it is due to existence of higher free volumes (according to free volume results in *Free volume characteristic*) created by loading of functionalized CNT
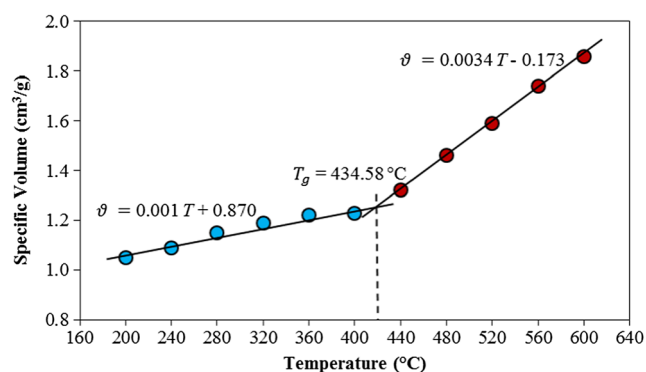
Fig. 6 Specific volume as a function of temperature for calculating T_g of [PIM/*f*-MWCNT(0.5%)] MMM

Table 8 The simulation results and the available experimental data of T_g at the temperature range (200–600 °C) for the simulated pure PIM membrane and its MMMs

Membranes	T_g (°C)
Pure PIM	428.47 (436[a])
[PIM/*p*-SWCNT(0.5%)] MMM	436.59
[PIM/*p*-SWCNT(1%)] MMM	437.46
[PIM/*p*-SWCNT(2%)] MMM	438.83
[PIM/*p*-SWCNT(3%)] MMM	436.82
[PIM/*f*-SWCNT(0.5%)] MMM	442.36
[PIM/*f*-SWCNT(1%)] MMM	443.79
[PIM/*f*-SWCNT(2%)] MMM	444.90
[PIM/*f*-SWCNT(3%)] MMM	443.41
[PIM/*p*-MWCNT(0.5%)] MMM	432.32
[PIM/*p*-MWCNT(1%)] MMM	433.00
[PIM/*p*-MWCNT(2%)] MMM	433.84
[PIM/*p*-MWCNT(3%)] MMM	432.68
[PIM/*f*-MWCNT(0.5%)] MMM	434.58
[PIM/*f*-MWCNT(1%)] MMM	435.79
[PIM/*f*-MWCNT(2%)] MMM	436.48
[PIM/*f*-MWCNT(3%)] MMM	435.31

[a] is the experimental value from [64]

particles into the PIM matrix. The T_g results (in Table 8) for either pristine or functionalized [PIM/SWCNT] MMMs have higher values than those of [PIM/MWCNT] MMMs. The reason for this difference can be explained by considering the fact that, in the same weight percent ratio (as seen in Table 2) of [CNT/(CNT + PIM)] for the [PIM/SWCNT] and [PIM/MWCNT] MMMs, the mass of MWCNT particles is much higher than that of the SWCNT particles therefore, the number density of SWNCT particles in the simulation cell is actually much higher than that of MWCNT particles. On the other hand, considering the *RDF* results presented in Fig. 5, it is seen that: the molecular interactions between PIM chains and SWCNT particles are stronger than MWCNT particles, and as a result the restriction on the chain mobility of PIM in [PIM/SWCNT] MMMs is more than [PIM/MWCNT] MMMs. The overall effect of these differences including the number density and molecular interaction between PIM chains and CNT (SWCNT and MWCNT) particles causes an increase in T_g values of [PIM/SWCNT] MMMs compared with those of [PIM/MWCNT] MMMs. It should be noted that, in all MMMs, due to thermal stability of the added CNT particles on increasing the CNTs content up to 2 wt%, the T_gs increase (Table 8), whereas at 3 wt% the T_g decreases. This behavior can be explained by the presence of defects due to agglomeration of CNT particles and reduction in the thermal stability of the MMMs which cause a decrease of interfacial interactions between CNT particles and PIM chains [13, 15, 16].

Free volume characteristic

In the structure of polymeric membranes two main phases are generally observed which include a solid phase polymer and a free volume [54, 57]. The free volume is due to chain packing which creates cavities and voids between the polymer chains in pure membranes and nano-gaps on the polymer/nanofillers interface in MMMs. The free volume provides diffusion paths for gas passage through the membranes [36, 39, 60, 67, 68] and therefore, affects the transport properties of the membranes.

The fractional free volume (FFV) is defined as [18, 50]:

$$FFV = \frac{V - V_O}{V} = \frac{V_F}{V} \qquad (1)$$

In Eq. 1, V is the simulation cell volume and V_O is the cell volume occupied by the membrane, which is defined as $V_O = 1.3\,V_{vdW}$, where V_{vdW} represents the van der Waals volume of the polymer chains and V_F the free volume is expressed as: $V_F = V - V_O$ [18, 50]. In this study, the simulation cell volume (V) for the desired membranes was obtained by utilizing the 'Amorphous Module' of the MS software [54]. In this module, the interaction between the membranes' components at the required fixed weight percent ratio, namely pure PIM chains or PIM chains and CNT particles, are taken into account by the proper force field as explained in *The force filed*, to construct and provide the simulation cell with the minimum space to accommodate the membrane, corresponding to its experimental

density, by employing 5 ns *NPT* MD simulation. It should be noted that in constructing simulation cell two factors are involved; the molecular size of components and their molecular interactions. The calculated values of V, V_O, V_{vdW}, V_F, and FFV for the studied membranes are reported in Table 9. The FFV values in this table are in good agreement with the reported experimental data [13]. In Fig. 7, the final molecular configurations of the simulation cells which show in blue color, the presence of free volume in the membranes, are clearly seen. The simulated results in Table 9 and Fig. 7 indicate an increment of FFV of the MMMs have occurred as a result of CNT particles loading into the PIM matrix which can be attributed to chain separations increase as well as chains packing disruption [13, 15]. This increment in the FFV values (in Table 9) for [PIM/SWCNT] MMMs is greater than [PIM/MWCNT] MMMs. The reason for this increment can be explained, as mentioned above, by considering two effective factors; the molecular size and molecular interaction. The size of MWCNT particles (inner diameter = 13.56 Å) is bigger than SWCNT particles (inner diameter = 6.78 Å) [48]. Also, the molecular interactions between PIM chains and MWCNT particles is weaker than those between PIM and SWCNT particles, as explained by considering the *RDF* results, presented in Fig. 5. Therefore, in the [PIM/MWCNT] MMMs, due to the larger size of MWCNT particles and the weaker interaction between PIM chains and MWCNT particles the values of V and V_F are greater than those of [PIM/SWCNT] MMMs. However, FFV as an intensive property is a

Table 9 The simulation cell volume (V), occupied volume (V_O), van der Waals volume (V_{vdW}), and free volume (V_F) as well as the fractional free volume (FFV) of the simulated pure PIM membrane and its MMMs along with the available experimental data for FFV

Membranes	V (Å³)	V_O (Å³)	V_{vdW} (Å³)	V_F (Å³)	FFV (%)
Pure PIM	274,510.07	216,313.94	166,395.33	58,196.13	21.20 (23.20[a], 22.80[b], 22.00[c])
[PIM/p-SWCNT(0.5%)] MMM	274,980.44	203,952.99	156,886.92	71,027.45	25.83
[PIM/p-SWCNT(1%)] MMM	275,447.58	203,996.48	156,920.37	71,451.10	25.94
[PIM/p-SWCNT(2%)] MMM	276,372.32	202,498.00	155,767.69	73,874.32	26.73
[PIM/p-SWCNT(3%)] MMM	277,284.55	206,410.62	158,777.40	70,873.93	25.56
[PIM/f-SWCNT(0.5%)] MMM	415,221.95	303,610.29	233,546.38	111,611.66	26.88
[PIM/f-SWCNT(1%)] MMM	418,661.54	305,915.98	235,319.99	112,745.55	26.93
[PIM/f-SWCNT(2%)] MMM	425,489.45	308,777.69	237,521.30	116,711.75	27.43
[PIM/f-SWCNT(3%)] MMM	433,727.14	316,447.32	243,421.02	117,279.82	27.04
[PIM/p-MWCNT(0.5%)] MMM	686,842.13	530,448.17	408,037.06	156,393.95	22.77
[PIM/p-MWCNT(1%)] MMM	687,404.19	524,626.88	403,559.14	162,777.31	23.68
[PIM/p-MWCNT(2%)] MMM	688,513.94	521,962.42	401,509.55	166,551.52	24.19
[PIM/p-MWCNT(3%)] MMM	689,604.90	524,513.49	403,471.91	165,091.41	23.94
[PIM/f-MWCNT(0.5%)] MMM	824,538.49	619,310.86	476,392.97	205,227.63	24.89
[PIM/f-MWCNT(1%)] MMM	825,538.68	619,071.46	476,208.81	206,467.22	25.01
[PIM/f-MWCNT(2%)] MMM	831,784.94	619,513.42	476,548.79	212,271.52	25.52
[PIM/f-MWCNT(3%)] MMM	833,696.62	624,272.03	480,209.25	209,424.59	25.12

[a] is the experimental value from [55]

[b] is the experimental value from [63]

[c] is the experimental value from [60]
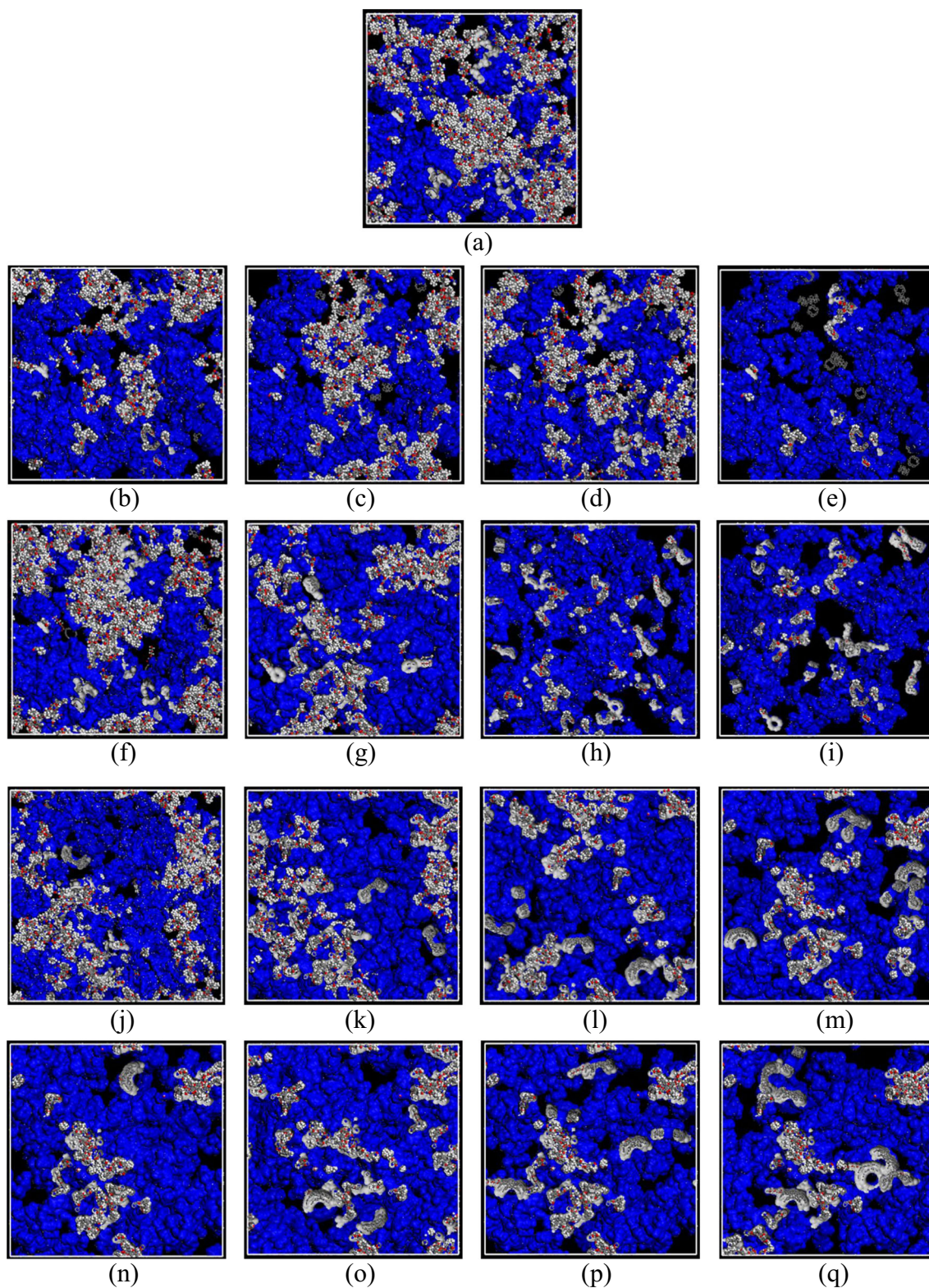
Fig. 7 Simulation cells of (a) Pure PIM, (b) [PIM/*p*-SWCNT(0.5%)], (c) [PIM/*p*-SWCNT(1%)], (d) [PIM/*p*-SWCNT(2%)], (e) [PIM/*p*-SWCNT(3%)], (f) [PIM/*f*-SWCNT(0.5%)], (g) [PIM/*f*-SWCNT(1%)], (h) [PIM/*f*-SWCNT(2%)], (i) [PIM/*f*-SWCNT(3%)], (j) [PIM/*p*-MWCNT(0.5%)], (k) [PIM/*p*-MWCNT(1%)], (l) [PIM/*p*-MWCNT(2%)], (m) [PIM/*p*-MWCNT(3%)], (n) [PIM/*f*-MWCNT(0.5%)], (o) [PIM/*f*-MWCNT(1%)], (p) [PIM/*f*-MWCNT(2%)], and (q) [PIM/*f*-MWCNT(3%)] MMMs with their free volume

commonly accepted criterion to judge the structural characteristics of the membrane, instead of V and V_F which are extensive properties. These structural characteristics include presence of spacing and voids between the components in the membrane which can provide pathways for diffusion and penetration of gas molecules into the membrane. Therefore, considering the results in Table 9, it is seen that as expected the obtained FFV values for all types of the studied MMMs are in the following order; $FFV_{[PIM/SWCNT]\ MMM} > FFV_{[PIM/MWCNT]\ MMM}$. Also, the FFV values in Table 9, for both pristine and functionalized MMMs indicate that they are in the following order; $FFV_{[PIM/f\text{-}SWCNT]\ MMM} > FFV_{[PIM/p\text{-}SWCNT]\ MMM}$ and $FFV_{PPIM/f\text{-}MWCNT]\ MMM} > FFV_{[PIM/p\text{-}MWCNT]\ MMM}$. This order can be explained by considering the fact that; the functionalized CNT particles disperse more smoothly in the PIM matrix, due to their stronger interactions with the PIM chains compared with those of pristine CNT particles. Therefore, the higher FFV values as reported in Table 9 for the MMMs containing functionalized CNT particles can be attributed to the presence of more voids between PIM chains and more nano-gaps at PIM/CNT interfaces, as observed experimentally by other researchers [13, 15, 46]. On the other hand, the addition of CNT particles from 0.5 to 2 wt% would increase the FFV of the resulting MMMs (Table 9 and Fig. 7) as a result of chains' packing distortion in the PIM matrix. However, by loading more than 3 wt% of pristine or functionalized CNT particles, due to their tendency for agglomeration at higher weight percent (as explained in *Equilibrium validation*), they are not smoothly distributed among the PIM chains and as a result the voids between PIM chains and nano-gaps at PIM/CNT interfaces have reduced which are manifested by decreasing the FFV values as presented in Table 9.

X-ray diffraction pattern

To investigate the crystalline properties of pure PIM and its MMMs, the X-ray diffraction (*XRD*) pattern of all simulated membranes were obtained by calculating the scattering intensity curve, $I(Q)$, through a Fourier transform operation of the radial distribution function as presented by the following Eq. [18, 50, 51]:

$$I(Q) = \sum_j \sum_k \frac{f_j f_k (\sin Q\ r_{jk})}{Q\ r_{jk}} \tag{2}$$

where the magnitude of the scattering angle, Q, is given by [18, 51]:

$$Q = \frac{4\ \pi\ \sin\theta}{\lambda} \tag{3}$$

In this equation, θ is the scattering angle and λ is the X-ray wavelength. The indices j and k range over all the atoms in the molecule [18, 50, 51]. Generally, considering the maximum peak in the diffraction pattern is important. Since by using it

along with the Bragg equation, $d = \lambda/2\ \sin\theta$, the corresponding d-spacing (d) values which indicate the intersegmental distances between the polymer backbones can be calculated. By applying the 'Forcite Modules' of the MS software [18], the XRDs of pure membrane and its MMMs were evaluated. The calculated intensity of XRD pattern versus X-ray incident angle (θ) at 30 °C temperature for the [PIM/p-SWCNT(1%)] MMM, as an example, is represented in Fig. 8. The obtained XRD results for other simulated membranes are summarized in Table 10. In Fig. 8, three different main broad peaks are observed which are due to the amorphous nature of the [PIM/p-SWCNT(1%)] MMM. The XRD results for pure PIM membrane in Table 10 indicate three characteristic peaks at $2\theta_1 = 12.84°$, $2\theta_2 = 19.03°$, and $2\theta_3 = 23.84°$ which respectively correspond to d-spacing of; $d_1 = 6.89$ Å, $d_2 = 4.66$ Å and $d_3 = 3.73$ Å. The first peak probably is assigned to the inefficient packing of PIM chains which originated from the sites of contortion in polymer backbone [28, 60]. The second peak results from the densely packed amorphous chains of PIM [28, 42, 60], and the third peak refers to the aromatic rings in the PIM structure [28, 42, 60]. By comparing the XRD results of MMMs with pure PIM, it is found that no significant change occurred in the first and third peaks, whereas the second amorphous broad peak for MMMs has shifted slightly left, which represents an increase in d_2 (d-spacing of the second peak). It means that by adding CNT particles into the PIM matrix, the intersegmental distance between PIM chains has increased. The increase in the intersegmental distance of PIM chains which caused an increase in the free volume (V_f) of MMMs (as reported in Table 9) was ascribed to the larger inner diameter of MWCNT particles compared to SWCNT particles and now in terms of d-spacing, it can be represented as: $d_{2_{PIM/MWCNT\ MMM}} > d_{2_{PIM/SWCNT\ MMM}}$. Also, the results in Table 10 indicate that, the d-spacing of functionalized CNT particles enhances, since PEG chains act as a spacer between PIM chains [13, 15].

Finally, by comparing the simulation results for T_g, V_F, and XRD, it can be stated that, in addition to the existence of good agreement between simulation results and available experimental data [13], a high matching between different simulation results as obtained in this work are observed for pure PIM
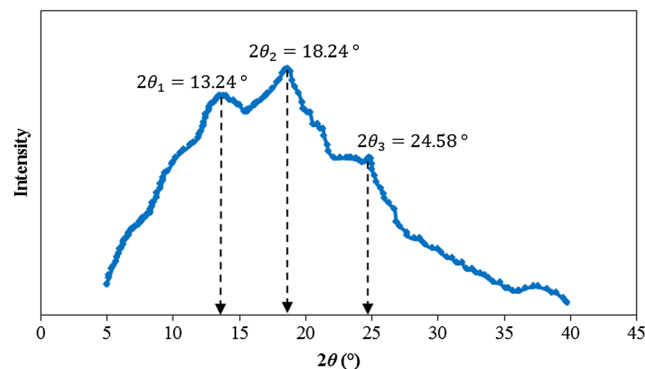

Fig. 8 The X-ray patterns of [PIM/p-SWCNT(1%)] MMM

membrane and its MMMs. For example, by comparison of the results for [PIM/f-MWCNT(2%)] and [PIM/f-SWCNT(2%)] MMMs in Tables 8, 9, and 10, it can be seen that: the T_g values (Table 8) for the [PIM/f-MWCNT(2%)] MMM are lower than [PIM/f-SWCNT(2%)] MMM, V_f values (Table 9) for [PIM/f-MWCNT(2%)] MMM are higher than for [PIM/f-SWCNT(2%)]) MMM, and finally, d_2 values (Table 10) for [PIM/f-MWCNT(2%)] MMM are higher than for [PIM/f-SWCNT(2%)]) MMM.

In the following section, we discuss the effect of physical properties (T_g, V_f, and d-spacing) of the membranes, as obtained so far in this work, on their transport properties by evaluating diffusivity, solubility, and permeability of pure gases (CO_2, CH_4, N_2, and O_2) as well as the membranes' selectivity for the binary mixtures of these gases.

Transport properties

Diffusivity

In the MD simulation, the diffusivity (D, cm^2/s) of a penetrant gas can be calculated by using the Einstein relationship which is in the following form [52, 57]:

$$D = \frac{1}{6} \frac{1}{N} \lim_{t \to \infty} \frac{d}{dt} \left\langle |r(t) - r(0)|^2 \right\rangle \qquad (4)$$

where N is the number of diffusing atoms i, r is the position vector of a gas molecule and $\left\langle |r(t) - r(0)|^2 \right\rangle$ represents the ensemble average of the mean square displacement (MSD) of the gas molecule trajectory in the simulation cell over the time interval t. The gas molecule trajectory was calculated by applying NVT MD simulation and by using the 'Discover Module' of MS software [48, 54] in a simulation time of 5 ns. The Einstein relationship (Eq. 4) assumes a random walk for the diffusing gas molecules. However, in the first stage of diffusion and in the short time intervals, when the gas molecules diffuse slowly the anomalous diffusion regime is observed and is characterized by [18, 49, 59]:

$$\left\langle |r(t) - r(0)|^2 \right\rangle \propto t^n \qquad (5)$$

where n for anomalous regime is less than unity ($n_A < 1$). If the simulation time is longer than the hydrodynamic limit and is sufficiently long, a transition from anomalous to Einstein diffusion regime may be observed which is manifested by a linear relationship between MSD and t, and the value of n in Eq. 5 goes to unity ($n_E \sim 1$) [18].

To calculate the diffusivity of CO_2, CH_4, N_2, and O_2 gases in the simulated pure PIM and its MMMs, at the first stage, the geometry optimization, energy minimization, and 500 ps NPT MD run were performed on each pure gas molecule, to

Table 10 The simulation results and the available experimental data for X-ray diffraction (XRD) patterns of the simulated pure PIM membrane and its MMMs

Membranes	2θ(°)			d-spacing (Å)		
	$2\theta_1$	$2\theta_2$	$2\theta_3$	d_1	d_2	d_3
Pure PIM	12.84 (13.00[a], 13.10[b])	19.03 (18.30[a], 18.20[b])	23.84 (22.60[b])	6.89(6.50[a], 6.70[b])	4.66 (4.84[a], 4.90[b])	3.73 (3.90[b])
[PIM/p-SWCNT(0.5%)] MMM	12.69	18.62	22.72	6.97	4.76	3.91
[PIM/p-SWCNT(1%)] MMM	13.24	18.42	24.58	6.68	4.81	3.62
[PIM/p-SWCNT(2%)] MMM	12.95	18.02	23.40	6.83	4.92	3.80
[PIM/p-SWCNT(3%)] MMM	12.80	18.15	23.65	6.91	4.88	3.76
[PIM/f-SWCNT(0.5%)] MMM	12.95	17.99	22.68	6.83	4.93	3.92
[PIM/f-SWCNT(1%)] MMM	12.59	17.93	22.61	7.03	4.94	3.93
[PIM/f-SWCNT(2%)] MMM	12.71	17.47	23.46	6.96	5.07	3.79
[PIM/f-SWCNT(3%)] MMM	12.85	17.83	23.89	6.88	4.97	3.72
[PIM/p-MWCNT(0.5%)] MMM	12.71	17.14	23.13	6.96	5.17	3.84
[PIM/p-MWCNT(1%)] MMM	12.76	17.09	23.19	6.93	5.18	3.83
[PIM/p-MWCNT(2%)] MMM	13.09	17.08	23.40	6.76	5.19	3.80
[PIM/p-MWCNT(3%)] MMM	13.05	17.34	23.63	6.78	5.11	3.76
[PIM/f-MWCNT(0.5%)] MMM	12.76	16.87	22.89	6.93	5.25	3.88
[PIM/f-MWCNT(1%)] MMM	13.10	16.76	23.42	6.75	5.29	3.80
[PIM/f-MWCNT(2%)] MMM	13.08	16.53	23.59	6.76	5.36	3.77
[PIM/f-MWCNT(3%)] MMM	12.98	16.53	23.79	6.82	5.36	3.74

[a] is the experimental value from [28]

[b] is the experimental value from [60]

make them achieve their equilibrium state. Then five molecules of each studied gas (CO_2, CH_4, N_2 or O_2) were embedded in the studied simulation cells containing either pure PIM or MMMs. The *MSD* of each pure penetrating gas molecule into the simulated membranes were calculated from their trajectories in the simulation cells. The average of five calculated diffusivity results was evaluated, for each pure gas by using Eq. 4, and is reported in Table 11. Also as an example, the *MSD* values versus simulation time for the studied gases (CO_2, CH_4, N_2, and O_2) in the constructed simulation cell of [PIM/p-MWCNT(1%)] MMM at 30 °C and 2 bar are shown in Fig. 9. To confirm that all the diffusivity results were calculated in the Einstein diffusion regime (i.e, $n_E \geq 1$) and to ensure that the adjusted simulation time at 5000 ps was sufficient to pass from the anomalous diffusion regime (i.e, $n_A < 1$) to the Einstein diffusion regime (i.e, $n_E \geq 1$), the values of n for the studied gases in the simulated cells along with the transition simulation time from anomalous diffusion regime to Einstein diffusion regime (t_t) are presented in Table 12. This table exhibits that for all the studied gases in the simulation cells $n_E \cong 1$ for $t_t < 3600$ ps. Therefore, it can be stated that the calculated diffusivity results satisfy the Einstein diffusion regime and are reliable. It should be noted that the diffusivity results as reported in Table 11 are in agreement with the experimental data [13]. Also, the evaluated diffusivity results for the studied gases in pure PIM membrane and its

MMMs are in the order of: $D_{O_2} > D_{CO_2} > D_{N_2} > D_{CH_4}$. This order of diffusivity results are in accord with the molecular size (σ) of the penetrated gases (Table 5). Previous investigations indicate that the diffusivity of gases through the polymeric membranes depends on two main factors, which are T_g and *FFV* [4, 67]. Comparing the results for T_g, *FFV* and D, as respectively reported in Tables 8, 9, and 11, indicates that the D values are highly dependent on *FFV* rather than T_g values. The reason for this can be explained by considering the fact that due to high T_g values of the studied membranes ($T_g > 400$ °C) and as a result, the restriction in the segmental rotations of PIM chains insufficiently large pathways are created between the chains by thermal motion to facilitate the gas diffusion through the simulated membranes [4, 25, 26, 28, 69, 70].

As an example, the trajectories of the studied gas molecules diffusing into the [PIM/p-MWCNT(1%)] MMM are presented in Fig. 10. Similar figures can be obtained for other studied membranes in this work. Figure 10 indicates that the gas molecules while diffusing into the membrane pass through created voids between the polymer chains as a result of polymer chain thermal motions. Due to this thermal motion the proper pathways for easy passage of gas molecules into the membranes are opened. The gas molecules entering into a void will oscillate. If the oscillation energy of the molecule is sufficient it will jump from one void to the neighboring one, otherwise it

Table 11 The simulation results (Sim.) and available experimental data (Exp. [13]) of diffusivity (10^7 cm^2/s) for CO_2, CH_4, N_2 and O_2 in the simulated pure PIM membrane and its MMMs at 30 °C temperature and 2 bar pressure

Membranes	CO_2		CH_4		N_2		O_2	
	Sim.	Exp.	Sim.	Exp.	Sim.	Exp.	Sim.	Exp.
Pure PIM	8.34 ± 1.09	7.91	2.44 ± 0.35	2.31	7.54 ± 1.25	7.15	24.14 ± 4.16	22.90
[PIM/p-SWCNT(0.5%)] MMM	19.43 ± 2.12	na	5.67 ± 0.79	na	17.56 ± 2.68	na	56.25 ± 5.34	na
[PIM/p-SWCNT(1%)] MMM	21.87 ± 2.23	na	6.39 ± 0.75	na	19.77 ± 2.96	na	63.32 ± 6.57	na
[PIM/p-SWCNT(2%)] MMM	23.76 ± 3.21	na	6.94 ± 0.45	na	21.48 ± 3.35	na	68.79 ± 7.64	na
[PIM/p-SWCNT(3%)] MMM	7.65 ± 1.25	na	2.23 ± 0.62	na	6.91 ± 1.60	na	22.15 ± 3.37	na
[PIM/f-SWCNT(0.5%)] MMM	20.04 ± 3.76	na	5.85 ± 0.45	na	18.11 ± 1.73	na	58.02 ± 6.42	na
[PIM/f-SWCNT(1%)] MMM	22.23 ± 3.43	na	6.49 ± 0.67	na	20.09 ± 2.12	na	64.36 ± 7.38	na
[PIM/f-SWCNT(2%)] MMM	24.76 ± 4.78	na	7.23 ± 0.09	na	22.38 ± 2.34	na	71.68 ± 7.64	na
[PIM/f-SWCNT(3%)] MMM	8.54 ± 1.38	na	2.49 ± 0.76	na	7.72 ± 0.56	na	24.72 ± 3.23	na
[PIM/p-MWCNT(0.5%)] MMM	8.59 ± 1.90	na	2.49 ± 0.35	na	7.86 ± 1.75	na	24.17 ± 4.35	na
[PIM/p-MWCNT(1%)] MMM	8.67 ± 1.54	na	2.53 ± 0.79	na	8.04 ± 0.43	na	25.67 ± 5.78	na
[PIM/p-MWCNT(2%)] MMM	10.54 ± 1.57	na	3.08 ± 0.75	na	9.53 ± 1.47	na	30.51 ± 6.88	na
[PIM/p-MWCNT(3%)] MMM	6.98 ± 1.87	na	2.04 ± 0.31	na	6.31 ± 1.77	na	20.21 ± 3.43	na
[PIM/f-MWCNT(0.5%)] MMM	10.54 ± 1.68	9.45	3.08 ± 0.58	2.35	9.53 ± 1.63	8.68	30.51 ± 4.47	26.20
[PIM/f-MWCNT(1%)] MMM	11.97 ± 1.90	13.70	3.50 ± 0.62	5.56	10.82 ± 2.21	12.80	34.65 ± 4.84	31.30
[PIM/f-MWCNT(2%)] MMM	18.23 ± 2.54	19.40	5.32 ± 0.48	10.30	16.48 ± 2.25	21.20	52.78 ± 5.32	46.40
[PIM/f-MWCNT(3%)] MMM	8.36 ± 1.56	6.72	2.44 ± 0.90	1.71	7.56 ± 1.78	5.18	24.20 ± 3.35	17.80

na: experimental data, not available
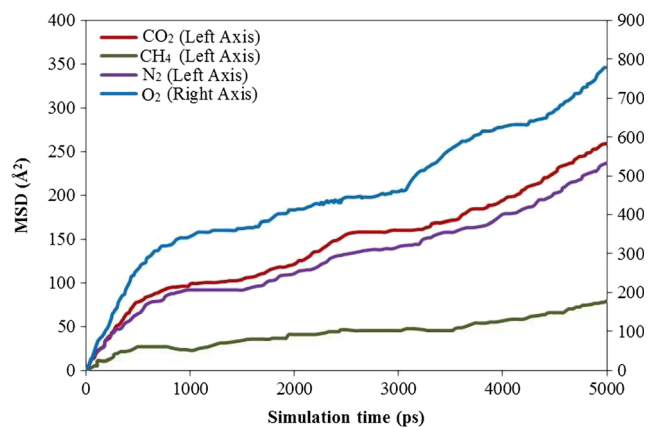
Fig. 9 The mean squared displacement (*MSD*) of CO_2, CH_4, N_2, and O_2 after 5 ns *NVT* MD simulations at 30 °C and 2 bar for [PIM/*p*-MWCNT(1%)] MMM versus simulation time

will remain trapped in the void. Considering Fig. 10, a large displacement indicates a jumping motion of a molecule from a void to a neighboring void, whereas a short displacement indicates an oscillating motion of a gas molecule in the void. This pattern of gas molecule diffusion is consistent with the proposed hopping mechanism for penetration of gases into the polymeric membranes. On comparing the gas displacement represented in Fig. 10, for the studied gases, it is seen that they are in the same order as their diffusivity results presented in Table 11 and discussed above in this section.

According to the diffusivity results for the studied MMMs (in Table 11), it is seen that the [PIM/SWCNT] MMMs have higher diffusivity in comparison to [PIM/MWCNT] MMMs. The higher diffusivity of [PIM/SWCNT] MMM is due to stronger interactions between PIM chains and the added SWCNT partilces as the nanofiller which would disrupt the polymer chain packing and create voids and nanoscale defects at the polymer/nanofillers interface. This behavior is manifested by higher *FFV* values of the MMMs and as a result facilitates the gas molecule passage through the created *FFV* by diffusion. However, functionalizing CNT particles by PEG does not increase the *FFV* of MMMs significantly (see Table 9). Therefore, the results indicate that functionalizing CNT particles enhances the diffusion of the studied gases into the functionalized membranes compared to pristine membranes but not significantly. It should be noted that after loading of 0.5 to 2 wt% CNT partilces, in all the MMMs, the diffusivity results of the studied gases increases which is due to the existence of continuous interface between CNT particles and polymer chains at lower CNTs loading [13]. However, at 3 wt% CNT particles loading, the diffusivities of gases decrease which is due to discontinuity of nano-gaps between CNTs and polymer chains as created by agglomeration of CNTs in between the PIM chains and as a result imposes a resistance to diffusion of gases into the MMMs [13, 15]. It seems that, this discontinuity does not occur when the CNT weight percent of is less than 3%.

Solubility

By applying the grand canonical Monte Carlo simulation (GCMC) and 'Sorption Module' of the MS software, according to the previously explained procedure [18, 50, 51], the solubility of pure CO_2, CH_4, N_2, and O_2 in the pure PIM membrane and its MMMs was calculated. The characteristics of the simulation cell are the same as used in MD simulations and are presented in Tables 2, 6, and 7. To perform the GCMC simulation calculations, the pure gas molecules were randomly embedded in the simulation cells. To simulate the solubility in the membrane, a gas molecule can be translated, rotated, created, and destroyed at random probabilities [51]. The basic equations for expressing the probabilities in the solubility calculations by using GCMC simulation are in the following form [18]:

$$P_{acc}(old \rightarrow new) = \min\left[1; \exp\left(-\frac{\Delta E}{k_B\,T} - \ln\frac{(N_i+1)\,k_B\,T}{f_i\,V}\right)\right] \quad (6)$$

where P_{acc} represents the acceptance criterion as evaluated by minimization of the right hand side of the above equation, according to the well-known Metropolis algorithm [18]. In Eq. 6, ΔE is the energy change due to converting an old configuration to a new one as a result of gas penetration into the membrane. Also, in this equation, k_B is the Boltzmann constant and T is the Kelvin temperature. Also, in Eq. 6, f_i and N_i are respectively the fugacity and the number molecules of component i (CO_2, CH_4, N_2, and O_2) in the gas phase and V is the volume of the simulation cell. The solubility of a gas i in the membrane, S_i (cm^3 gas (STP)/cm^3 polymer cmHg), is evaluated by using the following Eq. [18, 50]:

$$S_i = \lim_{p \to 0}\left(\frac{C_i}{p}\right) \quad (7)$$

where C_i (cm^3 gas (STP)/cm^3 polymer), is the concentration of the gas i, and p is the total pressure (cmHg). For the sake of comparison the pressure (0 to 760 cmHg) and temperature (30 °C) of the GCMC simulation in the solubility calculations were adjusted according to the reported experimental results [13]. At each pressure, 1,000,000 steps of GCMC calculations were performed to achieve the equilibration at a period of 100,000 steps. As an example, the calculated solubility results (C_i) according to Eq. 7 of the studied gases in the [PIM/*f*-MWCNT(1%)] MMM versus pressure variation (p) are plotted in Fig. 11. For other membranes the solubility results are reported in Table 13. Inspecting these results indicates that, the order of solubility of the studied gases in the simulated membranes is: $S_{CO_2} > S_{CH_4} > S_{O_2} > S_{N_2}$ which is in good agreement with the reported experimental data [13]. From Fig. 11 it is evident that the concentration of pure gases (CO_2, CH_4, O_2, and N_2) in the membranes increases with pressure and reaches equilibrium at higher pressure. This is consistent with

Table 12 The values of n in Eq. 5 at anomalous diffusion regime (n_A) and Einstein diffusion regime (n_E) along with the transition simulation time (t_t) for CO_2, CH_4, N_2, and O_2 in the simulated pure PIM membrane and its MMMs

Membranes	CO₂			CH₄			N₂			O₂		
	n_A	n_E	t_t	n_A	n_E	t_t	n_A	n_E	t_t	n_A	n_E	t_t
Pure PIM	0.63 ± 0.12	1.09 ± 0.24	3585	0.58 ± 0.45	1.14 ± 0.43	3436	0.48 ± 0.21	1.22 ± 0.57	3197	0.52 ± 0.35	1.16 ± 0.37	2873
[PIM/p-SWCNT(0.5%)] MMM	0.49 ± 0.17	1.07 ± 0.36	2868	0.47 ± 0.15	1.21 ± 0.36	2996	0.33 ± 0.14	1.07 ± 0.35	2903	0.54 ± 0.22	1.30 ± 0.16	3114
[PIM/p-SWCNT(1%)] MMM	0.53 ± 0.03	1.07 ± 0.21	3212	0.43 ± 0.22	0.93 ± 0.22	2875	0.39 ± 0.10	1.18 ± 0.38	2863	0.54 ± 0.14	1.14 ± 0.21	3340
[PIM/p-SWCNT(2%)] MMM	0.69 ± 0.12	1.49 ± 0.38	3302	0.75 ± 0.45	1.15 ± 0.25	3557	0.41 ± 0.15	0.91 ± 0.11	3390	0.29 ± 0.23	0.92 ± 0.22	3359
[PIM/p-SWCNT(3%)] MMM	0.65 ± 0.08	1.06 ± 0.14	3061	0.76 ± 0.26	1.33 ± 0.46	3288	0.43 ± 0.10	0.97 ± 0.26	3524	0.34 ± 0.16	0.94 ± 0.15	3078
[PIM/f-SWCNT(0.5%)] MMM	0.47 ± 0.21	0.93 ± 0.23	3254	0.52 ± 0.13	1.26 ± 0.24	3089	0.36 ± 0.22	1.07 ± 0.15	3368	0.35 ± 0.25	0.96 ± 0.25	3454
[PIM/f-SWCNT(1%)] MMM	0.42 ± 0.16	1.12 ± 0.17	3029	0.71 ± 0.47	1.09 ± 0.36	3291	0.35 ± 0.18	1.01 ± 0.11	3419	0.24 ± 0.17	1.02 ± 0.17	3421
[PIM/f-SWCNT(2%)] MMM	0.18 ± 0.08	1.11 ± 0.09	3242	0.49 ± 0.14	1.31 ± 0.21	3095	0.16 ± 0.12	1.01 ± 0.13	3467	0.21 ± 0.35	0.94 ± 0.21	2894
[PIM/f-SWCNT(3%)] MMM	0.39 ± 0.10	1.01 ± 0.32	2846	0.41 ± 0.36	1.04 ± 0.	3597	0.51 ± 0.05	1.00 ± 0.11	3116	0.44 ± 0.13	1.07 ± 0.12	2978
[PIM/p-MWCNT(0.5%)] MMM	0.24 ± 0.17	0.99 ± 0.34	3530	0.36 ± 0.09	1.03 ± 0.23	3387	0.57 ± 0.12	1.00 ± 0.21	3138	0.56 ± 0.13	1.04 ± 0.03	3508
[PIM/p-MWCNT(1%)] MMM	0.41 ± 0.15	1.06 ± 0.34	3136	0.42 ± 0.54	1.04 ± 0.34	3578	0.40 ± 0.18	1.08 ± 0.32	2987	0.45 ± 0.05	1.06 ± 0.09	3044
[PIM/p-MWCNT(2%)] MMM	0.75 ± 0.45	1.03 ± 0.56	3245	0.34 ± 0.13	0.98 ± 0.21	2904	0.41 ± 0.34	0.98 ± 0.34	3333	0.50 ± 0.13	0.97 ± 0.04	3198
[PIM/p-MWCNT(3%)] MMM	0.49 ± 0.14	0.99 ± 0.78	3596	0.54 ± 0.25	1.01 ± 0.09	3125	0.52 ± 0.31	1.02 ± 0.21	3389	0.40 ± 0.14	1.04 ± 0.12	3414
[PIM/f-MWCNT(0.5%)] MMM	0.29 ± 0.23	0.99 ± 0.34	3479	0.45 ± 0.12	0.98 ± 0.12	3443	0.43 ± 0.24	1.04 ± 0.13	3438	0.43 ± 0.02	1.05 ± 0.11	3577
[PIM/f-MWCNT(1%)] MMM	0.54 ± 0.22	1.03 ± 0.58	3343	0.52 ± 0.09	1.01 ± 0.32	2931	0.50 ± 0.12	1.00 ± 0.21	3467	0.47 ± 0.30	1.01 ± 0.10	3050
[PIM/f-MWCNT(2%)] MMM	0.48 ± 0.21	1.01 ± 0.77	2816	0.36 ± 0.03	0.97 ± 0.09	2882	0.55 ± 0.09	1.01 ± 0.35	3329	0.45 ± 0.14	1.00 ± 0.09	3153
[PIM/f-MWCNT(3%)] MMM	0.49 ± 0.17	1.07 ± 0.84	3074	0.34 ± 0.04	1.01 ± 0.03	3199	0.41 ± 0.08	1.05 ± 0.08	2858	0.37 ± 0.12	1.05 ± 0.14	2959
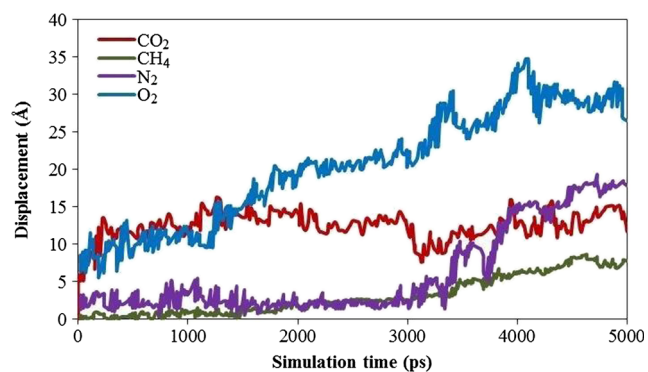
Fig. 10 The displacement of CO_2, CH_4, N_2, and O_2 in [PIM/p-MWCNT(1%)] MMM versus simulation time at 30 °C and 2 bar

Langmuir and Henry's law sorption models which as a combination are known as the dual sorption model [52, 65]. However, as seen in Fig. 11, the increment of CO_2 concentration is a strong convex curve, whereas for CH_4, N_2, and O_2 this is a smooth convex curve. The reason for this difference can be explained by considering the condensability of the studied gases [52]. The condensability of a gas is generally related to its critical temperature (T_c) and Lenard-Jones interaction parameter (ε/κ_B) [52, 65]. The values of T_c and ε/κ_B for the studied gases (CO_2, CH_4, N_2, and O_2) are presented in Table 5 which indicate that, they are in the same order of magnitude as those of solubility results. It is evident that CO_2 has the highest condensability (highest T_c and ε/κ_B) and therefore highest solubility in all the simulated membranes, whereas N_2 has the lowest condensability and then lowest solubility.
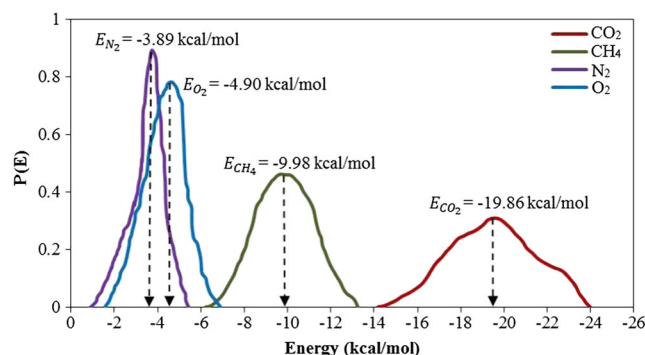
In addition to the condensability of gases which governs the gas solubility there are two other factors which may affect the gas solubility into the membranes, namely (*i*) the interactions between gas molecules and polymer chains as manifested by adsorption energy distribution and (*ii*) the interaction between gas molecules and the adsorption sites in the membrane matrix, manifested by adsorption density distribution of gases in the membrane matrix [23, 65, 66].
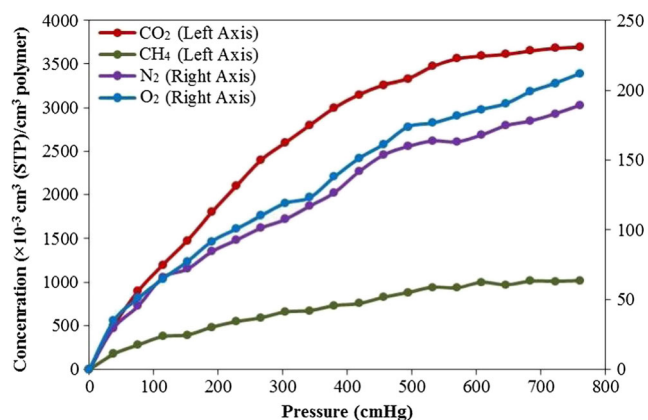
These two factors can be evaluated only by theoretical means such as GCMC simulation by using Eq. 6. The interaction energy of adsorption in GCMC simulation is defined as the accepted interaction energy of a gas molecule with the adsorbent matrix (PIM + CNTs) as represented in Eq. 6, where $\Delta E = E_{New} - E_{Old}$. If $\Delta E < 0$, the calculated E_{New} will be accepted and saved (as interaction energy of adsorption) by the "Sorption Module" of MS software [54] in the course of GCMC simulation. Figures 12 and 13 show respectively the calculated adsorption energy distribution and adsorption density distribution of CO_2, CH_4, N_2, and O_2 in [PIM/f-MWCNT(1%)] MMM by GCMC simulations. As seen in Fig. 12 there are four peaks at −19.86, −9.98, −3.89, and −4.90 kcal mol^{-1} respectively for CO_2, CH_4, N_2, and O_2. These adsorption energy values reveal that, due to the higher interaction of CO_2 with [PIM/f-MWCNT(1%)] MMM, the affinity for the adsorption of this gas in the MMM is higher than the other studied gases (CH_4, N_2, and O_2), and as a result, it has higher solubility. These results are in agreement with those obtained by GCMC simulation method for solubility of CO_2 and CH_4 in pure SWCNT, where it was found that due to stronger interaction between CO_2 and pure SWCNT it had higher solubility compared with that of CH_4 [71]. In Fig. 13 the red points represent the density distribution of the gases on the adsorption sites of the simulation cell of [PIM/f-MWCNT(1%)] MMM. As seen in this figure the number of the adsorption sites in this membrane is in the order of: $CO_2 > CH_4 > O_2 > N_2$ which is consistent with the calculated polymer-gas interaction energy as shown in Fig. 12.

Comparing the simulated solubility results of pure PIM membrane with those obtained for MMMs indicates no significant difference. However, by functionalizing the CNT particles with PEG, the CO_2 solubility increases gradually at the loadings of 0.5–3 wt%. The reason for this can be explained by considering the affinity of the resulting functionalized MMMs for adsorption of quadrupolar CO_2 molecules due to the presence of polar hydroxyl group of PEG [13, 15].

Fig. 11 The concentration of studied gases (CO_2, CH_4, N_2, and O_2) in [PIM/f-MWCNT(1%)] MMM at 30 °C and 0–760 cmHg

Fig. 12 Adsorption energy distribution of studied gases (CO_2, CH_4, N_2, and O_2) in [PIM/f-MWCNT(1%)] MMM at 30 °C and 0–760 cmHg

Table 13 The simulation results (Sim.) and available experimental data (Exp. [13]) of solubility (10^3 cm^3(STP)/cm^3(polymer) cmHg) for CO_2, CH_4, N_2, and O_2 in the simulated pure PIM membrane and its MMMs at 30 °C temperature and 2 bar

Membranes	CO_2		CH_4		N_2		O_2	
	Sim.	Exp.	Sim.	Exp.	Sim.	Exp.	Sim.	Exp.
Pure PIM	735.65 ± 132.45	785.21	167.43 ± 23.65	173.59	30.64 ± 2.34	39.02	32.93 ± 1.35	40.52
[PIM/p-SWCNT(0.5%)] MMM	737.87 ± 98.43	na	168.12 ± 28.97	na	30.77 ± 5.76	na	33.07 ± 4.56	na
[PIM/p-SWCNT(1%)] MMM	742.65 ± 110.32	na	170.89 ± 45.35	na	31.27 ± 5.34	na	33.61 ± 5.43	na
[PIM/p-SWCNT(2%)] MMM	746.85 ± 67.97	na	175.87 ± 25.67	na	32.18 ± 5.78	na	34.59 ± 3.36	na
[PIM/p-SWCNT(3%)] MMM	749.98 ± 109.86	na	167.55 ± 35.78	na	30.66 ± 2.34	na	32.95 ± 1.87	na
[PIM/f-SWCNT(0.5%)] MMM	739.45 ± 145.86	na	189.56 ± 17.45	na	34.69 ± 3.78	na	37.28 ± 2.75	na
[PIM/f-SWCNT(1%)] MMM	741.54 ± 112.34	na	199.56 ± 48.69	na	36.52 ± 3.43	na	39.25 ± 3.78	na
[PIM/f-SWCNT(2%)] MMM	789.54 ± 89.43	na	203.65 ± 21.98	na	37.27 ± 4.67	na	40.05 ± 5.23	na
[PIM/f-SWCNT(3%)] MMM	795.34 ± 56.89	na	176.54 ± 34.69	na	32.31 ± 3.76	na	34.72 ± 1.86	na
[PIM/p-MWCNT(0.5%)] MMM	736.76 ± 173.75	na	166.87 ± 23.65	na	30.54 ± 2.35	na	32.82 ± 1.47	na
[PIM/p-MWCNT(1%)] MMM	741.34 ± 126.78	na	168.67 ± 34.67	na	30.87 ± 1.78	na	33.17 ± 2.76	na
[PIM/p-MWCNT(2%)] MMM	743.67 ± 68.96	na	171.35 ± 65.32	na	31.36 ± 2.35	na	33.70 ± 2.58	na
[PIM/p-MWCNT(3%)] MMM	745.45 ± 129.64	na	165.35 ± 23.45	na	30.26 ± 1.54	na	32.52 ± 4.24	na
[PIM/f-MWCNT(0.5%)] MMM	736.86 ± 114.79	797.35	187.43 ± 56.85	297.02	34.30 ± 2.45	36.29	36.86 ± 1.98	37.98
[PIM/f-MWCNT(1%)] MMM	738.54 ± 176.53	570.29	196.46 ± 32.45	141.19	35.95 ± 2.56	32.58	38.64 ± 3.45	33.67
[PIM/f-MWCNT(2%)] MMM	764.43 ± 57.89	632.68	200.36 ± 67.54	143.98	36.67 ± 2.57	33.63	39.41 ± 4.32	36.21
[PIM/f-MWCNT(3%)] MMM	773.87 ± 109.46	716.67	176.80 ± 34.56	173.10	32.35 ± 1.45	41.89	34.77 ± 3.63	44.89

na: experimental data, not available

Permeability

After evaluating the diffusivity (Table 11) and solubility (Table 13) of gases in the constructed polymeric membranes, the permeability (*P*, Barrer) of the studied gases into the membranes, as an important transport property of membranes, should be considered. The permeability is expressed by the following Eq. [2, 4, 36, 67, 72–74]:

$$P = D \times S \tag{8}$$

The calculated permeability results for the studied gases are presented in Table 14 which are in the order of $P_{CO_2} > P_{O_2} > P_{CH_4} > P_{N_2}$ for all simulated membranes. This table shows that the simulated results are in good agreement with the available experimental data [13] and this can be considered as strong evidence that MD and GCMC simulation techniques used respectively for evaluating the diffusivity and solubility of the studied gases are accurate and reliable methods. The simulated permeability results (in Table 14) reveal that by incorporating pristine and functionalized CNT particles with the PIM matrix, the permeability of the resulting membrane enhances and this can be due to disruption of the polymer chains packing as a result of interaction between the CNT particles and the PIM chains which increases the *FFV* of the MMMs. Also, functionalizing CNT particles with PEG, increases the intersegmental distance between PIM chains and enhances the gas permeability. Comparison of the permeability results in Table 14

for [PIM/SWCNT] and [PIM/MWCNT] MMMs indicates that despite lower T_g values of the former MMMs the permeability of the later MMMs are higher. This difference can be ascribed to higher *FFV* of [PIM/SWCNT] MMMs (Table 9). This point can be substantiated by considering Fig. 4(b-i) which indicates a smooth distribution of the SWCNT particles in the PIM matrix compared with Fig. 4(j-q) which indicate agglomeration of MWCNT particles. The results in Table 14 show that, the loading of 0.5 to 2 wt% CNT particles, increases the permeability of gases into the studied membranes. This behavior, as explained earlier for diffusivity results (*Diffusivity*), can be explained by the presence of continuous interface between CNT particles and PIM chains [13, 15, 16]. However, at 3 wt% loading of CNT particles, the permeability of all gases decreases, and this is due to the presence of nano-gaps between CNT particles and polymer chains which cause discontinuity in the PIM matrix structure and consequently increase the resistance to the gas permeation through the membranes [13, 15, 46].
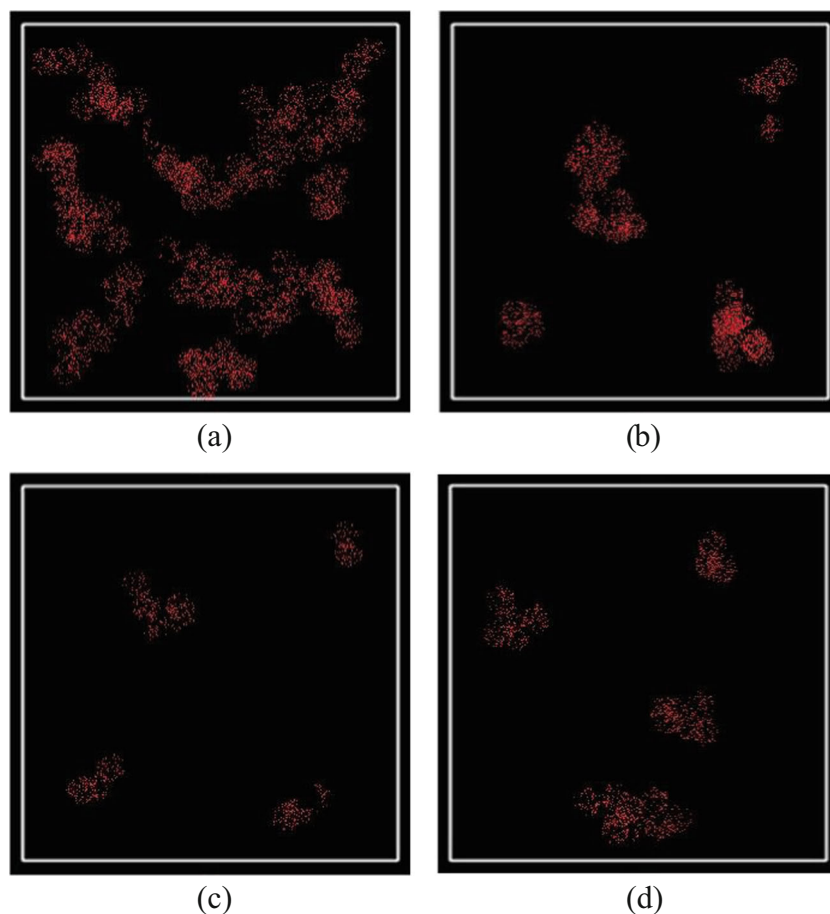
Selectivity

The selectivity ($\alpha_{A/B}$) is defined as [2–5, 29, 52, 73]:

$$\alpha_{A/B} = P_A/P_B \tag{9}$$

where *P* is the permeability expressed in Barrer (Eq. 8) for gases *A* and *B* in the membranes. The obtained results for the selectivity

Fig. 13 Adsorption density distribution of (a) CO_2, (b) CH_4, (c) N_2, and (d) O_2 in [PIM/f-MWCNT(1%)] MMM at 30 °C and 0–760 cmHg

(a)

(b)

(c)

(d)

as represented in Table 15 indicate that for the binary gas mixtures (CO_2/CH_4), (CO_2/N_2), and (CO_2/O_2) penetration into the studied membranes, the selectivity results are greater than unity, which means that by using these membranes, CO_2 can be separated from CH_4, N_2, and O_2. However, since for the (CH_4/N_2), (CH_4/O_2), and (N_2/O_2), the selectivity is close to unity, the

Table 14 The simulation results (Sim.) and available experimental data (Exp. [13]) of permeability (Barrer) for CO_2, CH_4, N_2, and O_2 in the simulated pure PIM membrane and MMMs at 30 °C temperature and 2 bar pressure

Membranes	CO_2		CH_4		N_2		O_2	
	Sim.	Exp.	Sim.	Exp.	Sim.	Exp.	Sim.	Exp.
Pure PIM	6135.32 ± 1325.66	6211	407.79 ± 137.43	401	248.25 ± 32.53	279	739.80 ± 143.67	928
[PIM/p-SWCNT(0.5%)] MMM	14,336.81 ± 2364.76	na	953.95 ± 236.86	na	580.74 ± 43.68	na	1730.64 ± 453.78	na
[PIM/p-SWCNT(1%)] MMM	16,241.76 ± 3754.78	15,721	1091.44 ± 348.88	1820	664.44 ± 56.74	949	1980.07 ± 432.86	2305
[PIM/p-SWCNT(2%)] MMM	17,745.16 ± 2374.97	na	1220.32 ± 348.75	na	742.89 ± 126.64	na	2213.87 ± 567.53	na
[PIM/p-SWCNT(3%)] MMM	5737.34 ± 528.65	na	374.32 ± 142.78	na	227.87 ± 13.68	na	679.08 ± 47.76	na
[PIM/f-SWCNT(0.5%)] MMM	14,818.58 ± 2748.67	na	1109.38 ± 325.89	na	675.36 ± 109.45	na	2012.61 ± 135.75	na
[PIM/f-SWCNT(1%)] MMM	16,484.43 ± 3267.64	na	1295.53 ± 532.78	na	788.68 ± 112.45	na	2350.32 ± 685.32	na
[PIM/f-SWCNT(2%)] MMM	19,549.01 ± 2747.78	na	1472.55 ± 238.64	na	896.44 ± 132.67	na	2671.47 ± 472.68	na
[PIM/f-SWCNT(3%)] MMM	6792.20 ± 1634.66	na	440.29 ± 34.78	na	268.03 ± 145.45	na	798.76 ± 45.78	na
[PIM/p-MWCNT(0.5%)] MMM	6328.76 ± 1343.56	na	415.43 ± 98.65	na	240.04 ± 23.8	na	793.26 ± 43.88	na
[PIM/p-MWCNT(1%)] MMM	6427.42 ± 945.78	6219	427.06 ± 32.78	757	248.19 ± 87.57	361	851.47 ± 36.78	957
[PIM/p-MWCNT(2%)] MMM	7838.24 ± 1238.53	na	527.42 ± 109.64	na	321.08 ± 135.97	na	956.84 ± 32.68	na
[PIM/p-MWCNT(3%)] MMM	5203.24 ± 458.21	na	337.05 ± 111.56	na	205.19 ± 93.55	na	611.47 ± 51.77	na
[PIM/f-MWCNT(0.5%)] MMM	7766.50 ± 845.89	7535	576.92 ± 134.78	698	351.21 ± 32.78	315	1046.63 ± 658.89	995
[PIM/f-MWCNT(1%)] MMM	8840.32 ± 1743.89	7813	686.76 ± 23.67	785	418.08 ± 55.97	417	1245.90 ± 542.78	1054
[PIM/f-MWCNT(2%)] MMM	13,935.56 ± 782.88	12,274	1066.68 ± 137.75	1483	649.36 ± 168.85	713	1935.14 ± 532.78	1680
[PIM/f-MWCNT(3%)] MMM	6469.55 ± 792.46	4816	431.64 ± 120.97	296	262.77 ± 136.79	217	783.07 ± 43.89	799

na: experimental data, not available

Table 15 The simulation results (Sim.) and available experimental data (Exp. [13]) of selectivity for binary gas mixtures (CO_2/CH_4), (CO_2/N_2), (CO_2/O_2), (CH_4/N_2), (CH_4/O_2), and (N_2/O_2) in the simulated pure PIM membrane and MMMs

Membranes	CO_2/CH_4		CO_2/N_2		CO_2/O_2		CH_4/N_2		CH_4/O_2		N_2/O_2	
	Sim.	Exp.	Sim.	Exp.	Sim.	Exp.	Sim.	Exp.	Sim.	Exp.	Sim.	Exp.
Pure PIM	9.21 ± 1.24	15.49	12.72 ± 2.45	22.26	4.17 ± 0.76	6.69	1.38 ± 0.43	1.44	0.45 ± 0.	0.43	0.33 ± 0.	0.30
[PIM/p-SWCNT(0.5%)] MMM	9.20 ± 1.34	na	15.25 ± 2.36	na	6.92 ± 1.87	na	1.66 ± 0.12	na	0.75 ± 0.06	na	0.45 ± 0.12	na
[PIM/p-SWCNT(1%)] MMM	9.11 ± 2.45	8.64	15.83 ± 2.12	16.57	7.28 ± 1.78	6.82	1.74 ± 0.56	1.92	0.80 ± 0.04	0.79	0.46 ± 0.09	0.41
[PIM/p-SWCNT(2%)] MMM	8.90 ± 1.87	na	14.85 ± 2.35	na	7.03 ± 0.45	na	1.67 ± 0.84	na	0.79 ± 0.07	na	0.47 ± 0.04	na
[PIM/p-SWCNT(3%)] MMM	9.08 ± 0.93	na	12.54 ± 2.67	na	4.11 ± 1.37	na	1.38 ± 0.90	na	0.45 ± 0.03	na	0.33 ± 0.11	na
[PIM/f-SWCNT(0.5%)] MMM	8.17 ± 1.23	na	12.92 ± 1.24	na	6.08 ± 1.48	na	1.58 ± 0.36	na	0.74 ± 0.03	na	0.47 ± 0.04	na
[PIM/f-SWCNT(1%)] MMM	7.79 ± 1.54	na	13.05 ± 2.46	na	6.07 ± 1.57	na	1.68 ± 0.31	na	0.78 ± 0.04	na	0.47 ± 0.05	na
[PIM/f-SWCNT(2%)] MMM	8.12 ± 2.34	na	12.34 ± 1.32	na	6.45 ± 1.73	na	1.52 ± 0.77	na	0.79 ± 0.09	na	0.52 ± 0.09	na
[PIM/f-SWCNT(3%)] MMM	9.44 ± 0.95	na	13.04 ± 0.95	na	4.54 ± 0.96	na	1.38 ± 0.60	na	0.48 ± 0.05	na	0.35 ± 0.03	na
[PIM/p-MWCNT(0.5%)] MMM	9.25 ± 1.54	na	11.04 ± 2.34	na	3.62 ± 1.42	na	1.19 ± 0.32	na	0.39 ± 0.05	na	0.33 ± 0.03	na
[PIM/p-MWCNT(1%)] MMM	9.21 ± 2.54	8.22	12.12 ± 1.36	17.23	3.98 ± 1.36	6.50	1.32 ± 0.64	2.10	0.43 ± 0.03	0.79	0.33 ± 0.08	0.38
[PIM/p-MWCNT(2%)] MMM	9.09 ± 1.95	na	14.16 ± 1.87	na	4.64 ± 0.45	na	1.56 ± 0.35	na	0.51 ± 0.03	na	0.33 ± 0.07	na
[PIM/p-MWCNT(3%)] MMM	9.13 ± 1.23	na	12.61 ± 0.43	na	4.14 ± 1.46	na	1.38 ± 0.78	na	0.45 ± 0.02	na	0.33 ± 0.04	na
[PIM/f-MWCNT(0.5%)] MMM	10.41 ± 2.34	10.80	12.82 ± 2.46	23.92	8.12 ± 1.36	7.57	1.23 ± 0.35	2.22	0.78 ± 0.04	0.70	0.63 ± 0.12	0.32
[PIM/f-MWCNT(1%)] MMM	9.72 ± 1.34	9.95	13.42 ± 2.14	18.74	8.01 ± 2.46	7.41	1.38 ± 0.62	1.88	0.82 ± 0.01	0.74	0.60 ± 0.09	0.40
[PIM/f-MWCNT(2%)] MMM	9.49 ± 1.56	8.28	19.08 ± 1.74	17.21	8.48 ± 1.35	7.31	2.01 ± 0.58	2.08	0.89 ± 0.02	0.88	0.44 ± 0.11	0.42
[PIM/f-MWCNT(3%)] MMM	12.75 ± 2.34	16.27	27.52 ± 0.45	22.19	12.76 ± 1.74	6.03	2.16 ± 0.27	1.36	1.00 ± 0.06	0.37	0.46 ± 0.07	0.27

na: experimental data, not available

constructed membranes are not suitable for separation of CH_4 from O_2 or N_2 and also separation of N_2 from O_2. Table 15 shows that the order of selectivity of the membranes is: $\alpha_{PIM/f-MWCNT\ MMM} > \alpha_{PIM/p-SWCNT\ MMM} > \alpha_{PIM/p-MWCNT\ MMM} > \alpha_{PIM/f-SWCNT\ MMM} > \alpha_{PIM}$ which means that the MMM consisting of [PIM/f-MWCNT] MMM has the highest selectivity for separation of CO_2 from CH_4, N_2, and O_2. However, the permeability results represented in *Permeability* indicate that [PIM/f-SWCNT] MMM has the highest permeability for CO_2. Therefore, by considering the effect of permeability-selectivity trade-off, it can be stated that the best choice is [PIM/f-SWCNT] MMM, for separation of CO_2 from CH_4, N_2, and O_2, among the studied MMMs.

Conclusions

In this work, five distinguished types (17 samples) of polymers of intrinsic microporosity (PIM) membranes were simulated by Materials Studio software. All the simulated membranes had PIM as their matrix but the type and the amounts of the added CNT particles to their matrix, were different. The abbreviations used to refer to the simulated membranes are presented in Table 1. To characterize the simulated membranes, the physical properties including density, glass transition temperature (T_g), X-ray diffraction pattern (*XRD*) and fractional free volume (*FFV*) were calculated. Then, the gas transport properties of the membranes such as diffusivity (D), solubility (S), and permeability (P) of pure gases (CO_2, CH_4, N_2, and O_2) as well as, the selectivity (α) of their binary mixtures (CO_2/CH_4), (CO_2/N_2), (CO_2/O_2), (CH_4/N_2), (CH_4/O_2), and (N_2/O_2) were evaluated which were consistent with the available experimental data. The results indicated that the transport properties for the penetrant gases through the studied pure PIM membrane and its mixed matrix membranes (MMMs), were in the following order: $D_{O_2} > D_{CO_2} > D_{N_2} > D_{CH_4}$, $S_{CO_2} > S_{CH_4} > S_{O_2} > S_{N_2}$ and $P_{CO_2} > P_{O_2} > P_{CH_4} > P_{N_2}$. These results were interpreted and discussed in terms of molecular size and condensability of gases and the physical properties of the membranes, such as T_g, *FFV*, and *XRD*. Considering the overall results indicated that the diffusivity and permeability of gases through the membranes for [PIM/SWCNT] MMMs were higher than [PIM/MWCNT] MMMs. Also, these properties for [PIM/f-SWCNT] MMMs and [PIM/f-MWCNT] MMMs were higher than [PIM/p-SWCNT] MMMs and [PIM/p-MWCNT] MMMs. It was found that the diffusivity and permeability of each membrane increased with the weight percent of CNT particles up to 2 wt% and then they started to decrease. However, the solubility results did not change by increasing CNT particles. The selectivity (α) results revealed that on addition of CNT particles, either pristine or functionalized, to the PIM matrix to obtain the MMMs, the ability of resulting membranes to separate quadrupolar gas (CO_2) from non-polar gases (CH_4, N_2, and O_2) in the binary gas mixtures increased in the following order: $\alpha_{PIM/f-MWCNT\ MMM} > \alpha_{PIM/p-SWCNT\ MMM} > \alpha_{PIM/p-MWCNT\ MMM} > \alpha_{PIM/f-SWCNT\ MMM} > \alpha_{PIM}$ which means that the MMM consisting of [PIM/f-MWCNT] MMM has the highest selectivity for separation of CO_2 from CH_4, N_2, and O_2. However, the permeability results indicate that [PIM/f-SWCNT] MMM has the highest permeability for CO_2. Therefore, by considering the effect of permeability-selectivity trade-off, it can be stated that the best choice is [PIM/f-SWCNT] MMM, for separation of CO_2 from CH_4, N_2, and O_2, among the studied MMMs.

l, Simulation cell length (Å); C, Concentration of gas molecules in the simulation cell (cm^3 gas (STP)/cm^3 polymer); D, Diffusivity (cm^2/s); E, Energy of configuration (kcal mol^{-1}); *FFV*, Fractional free volume; f_i, Fugacity of component i in the gas phase (bar); k_B, Boltzmann constant (bar m^3/K); n, Proportionality coefficient; n_A, Proportionality coefficient at anomalous diffusion regime; n_E, Proportionality coefficient at Einstein diffusion regime; N_i, Current number of component i molecules in the membrane cell; p, Total pressure (bar); P, Permeability (Barrer, 1 Barrer =10^{-10} cm^3(STP) cm/cm^2 s cmHg); P_{acc}, Acceptance probability; $r(t)$, Final position vectors of the center of mass of the gas molecules over the time interval t (Å); $r(0)$, Initial position vectors of the center of mass of the gas molecules (Å); S, Solubility (cm^3 gas (STP)/cm^3 polymer cmHg); t, Simulation time (ps); T, Temperature (K); T_g, Glass transition temperature (K); T_c, Critical temperature (K); V, Volume of membrane cell (Å^3); V_O, Occupied volume of the polymer chains (Å^3); V_{vdW}, van der Waals volume of the polymer chains (Å^3); V_F, Free volume (Å^3)

α_{AB}, Selectivity; ε κ_B, Lenard-Jones interaction parameter (K); σ, Lenard-Jones size parameter (Å)

PIM-1, Polymers of intrinsic microporosity; PEG, Polyethylene glycol; CNT, Carbon nanotube; SWCNT, Single-walled carbon nanotube; p-SWCNT, Pristine single-walled carbon nanotube; f-SWCNT, Functionalized single-walled carbon nanotube; MWCNT, Multi-walled carbon nanotube; p-MWCNT, Pristine multi-walled carbon nanotube; f-MWCNT, Functionalized multi-walled carbon nanotube

References

1. Adewole JK, Ahmad AL, Ismail S, Leo CP (2013) Current challenges in membrane separation of CO_2 from natural gas: a review. Int J Greenh Gas Control 17:46–65. doi:10.1016/j.ijggc.2013.04.012

2. Dai Z, Deng L (2016) Membrane absorption using ionic liquid for pre-combustion CO_2 capture at elevated pressure and temperature. Int J Greenh Gas Control 54(Part 1):59–69. doi:10.1016/j.ijggc.2016.09.001

3. Deng L, Hägg M-B (2014) Carbon nanotube reinforced PVAm/PVA blend FSC nanocomposite membrane for CO_2/CH_4 separation. Int J Greenh Gas Control 26:127–134. doi:10.1016/j.ijggc.2014.04.018

4. Gemeda AE, De Angelis MG, Du N, Li N, Guiver MD, Sarti GC (2017) Mixed gas sorption in glassy polymeric membranes. III. CO_2/CH_4 mixtures in a polymer of intrinsic microporosity (PIM-1): Effect of temperature. J Membr Sci 524:746–757. doi:10.1016/j.memsci.2016.11.053

5. Gui MM, Yap YX, Chai S-P, Mohamed AR (2013) Multi-walled carbon nanotubes modified with (3-aminopropyl)triethoxysilane for effective carbon dioxide adsorption. Int J Greenh Gas Control 14:65–73. doi:10.1016/j.ijggc.2013.01.004

6. Gomez-Coma L, Garea A, Irabien A (2016) Carbon dioxide capture by [emim][ac] ionic liquid in a polysulfone hollow fiber membrane contactor. Int J Greenh Gas Control 52:401–409. doi:10.1016/j.ijggc.2016.07.019

7. George G, Bhoria N, Alhallaq S, Abdala A, Mittal V (2016) Polymer membranes for acid gas removal from natural gas. Sep Purif Technol 158:333–356. doi:10.1016/j.seppur.2015.12.033

8. Camponeschi E, Vance R, Al-Haik M, Garmestani H, Tannenbaum R (2007) Properties of carbon nanotube–polymer composites aligned in a magnetic field. Carbon 45:2037–2046. doi:10.1016/j.carbon.2007.05.024

9. Castillo FY, Socher R, Krause B, Headrick R, Grady BP, Prada-Silvy R, Pötschke P (2011) Electrical, mechanical, and glass transition behavior of polycarbonate-based nanocomposites with different multi-walled carbon nanotubes. Polymer 52:3835–3845. doi:10.1016/j.polymer.2011.06.018

10. Dundar E, Chanut N, Formalik F, Boulet P, Llewellyn PL, Kuchta B (2017) Modeling of adsorption of CO_2 in the deformed pores of MIL-53(al). J Mol Model 23:101. doi:10.1007/s00894-017-3281-4

11. Cong H, Zhang J, Radosz M, Shen Y (2007) Carbon nanotube composite membranes of brominated poly (2, 6-diphenyl-1, 4-phenylene oxide) for gas separation. J Membr Sci 294:178–185. doi:10.1016/j.memsci.2007.02.035

12. Daraei P, Madaeni SS, Ghaemi N, Khadivi MA, Astinchap B, Moradian R (2013) Enhancing antifouling capability of PES membrane via mixing with various types of polymer modified multi-walled carbon nanotube. J Membr Sci 444:184–191. doi:10.1016/j.memsci.2013.05.020

13. Khan MM, Filiz V, Bengtson G, Shishatskiy S, Rahman MM, Lillepaerg J, Abetz V (2013) Enhanced gas permeability by fabricating mixed matrix membranes of functionalized multiwalled carbon nanotubes and polymers of intrinsic microporosity (PIM). J Membr Sci 436:109–120. doi:10.1016/j.memsci.2013.02.032

14. Kim S, Chen L, Johnson JK, Marand E (2007) Polysulfone and functionalized carbon nanotube mixed matrix membranes for gas separation: theory and experiment. J Membr Sci 294:147–158. doi:10.1016/j.memsci.2007.02.028

15. Khan MM, Filiz V, Bengtson G, Shishatskiy S, Rahman M, Abetz V (2012) Functionalized carbon nanotubes mixed matrix membranes of polymers of intrinsic microporosity for gas separation. Nanoscale Res Lett 7:504. doi:10.1186/1556-276X-7-504

16. Khan M, Filiz V, Bengtson G, Rahman M, Shishatskiy S, Abetz V (2012) Functionalized carbon nanotube mixed matrix membranes of polymers of intrinsic microporosity (PIMs) for gas separation. Procedia Eng 44:1899–1901. doi:10.1186/1556-276X-7-504

17. Liang G, Tjong S (2006) Electrical properties of low-density polyethylene/multiwalled carbon nanotube nanocomposites. Mater Chem Phys 100:132–137. doi:10.1016/j.matchemphys.2005.12.021

18. Golzar K, Amjad-Iranagh S, Amani M, Modarress H (2014) Molecular simulation study of penetrant gas transport properties into the pure and nanosized silica particles filled polysulfone membranes. J Membr Sci 451:117–134. doi:10.1016/j.memsci.2013.09.056

19. Mckeown NB, Budd PM, Msayib K, Ghanem B (2011) Microporous polymer material. Google Patents.

20. Mckeown N, Maksheed S (2002) Organic microporous materials. Google Patents.

21. Ahn J, Chung W-J, Pinnau I, Song J, Du N, Robertson GP, Guiver MD (2010) Gas transport behavior of mixed-matrix membranes composed of silica nanoparticles in a polymer of intrinsic microporosity (PIM-1). J Membr Sci 346:280–287. doi:10.1016/j.memsci.2008.01.031

22. Budd PM, Mckeown NB, Ghanem BS, Msayib KJ, Fritsch D, Starannikova L, Belov N, Sanfirova O, Yampolskii Y, Shantarovich V (2008) Gas permeation parameters and other physicochemical properties of a polymer of intrinsic microporosity: Polybenzodioxane PIM-1. J Membr Sci 325:851–860. doi:10.1016/j.memsci.2008.09.010

23. Budd PM, Msayib KJ, Tattershall CE, Ghanem BS, Reynolds KJ, Mckeown NB, Fritsch D (2005) Gas separation membranes from polymers of intrinsic microporosity. J Membr Sci 251:263–269. doi:10.1016/j.memsci.2005.01.009

24. Heuchel M, Fritsch D, Budd PM, Mckeown NB, Hofmann D (2008) Atomistic packing model and free volume distribution of a polymer with intrinsic microporosity (PIM-1). J Membr Sci 318:84–99. doi:10.1016/j.memsci.2008.02.038

25. Salinas O, Ma X, Litwiller E, Pinnau I (2016) Ethylene/ethane permeation, diffusion and gas sorption properties of carbon molecular sieve membranes derived from the prototype ladder polymer of intrinsic microporosity (PIM-1). J Membr Sci 504:133–140. doi:10.1016/j.memsci.2015.12.052

26. Vopička O, De Angelis MG, Du N, Li N, Guiver MD, Sarti GC (2014) Mixed gas sorption in glassy polymeric membranes: II. CO_2/CH_4 mixtures in a polymer of intrinsic microporosity (PIM-1). J Membr Sci 459:264–276. doi:10.1016/j.memsci.2014.02.003

27. Vopička O, Friess K, Hynek V, Sysel P, Zgažar M, Šípek M, Pilnáček K, Lanč M, Jansen JC, Mason CR (2013) Equilibrium and transient sorption of vapours and gases in the polymer of intrinsic microporosity PIM-1. J Membr Sci 434:148–160. doi:10.1016/j.memsci.2013.01.040

28. Zhao H, Xie Q, Ding X, Chen J, Hua M, Tan X, Zhang Y (2016) High performance post-modified polymers of intrinsic microporosity (PIM-1) membranes based on multivalent metal ions for gas separation. J Membr Sci 514:305–312. doi:10.1016/j.memsci.2016.05.013

29. Kim K, Lee S, Ryu JH, Lee KS, Lee WB (2013) An improved CO_2 adsorption efficiency for the zeolites impregnated with the amino group: A molecular simulation approach. Int J Greenh Gas Control 19:350–357. doi:10.1016/j.ijggc.2013.09.013

30. Wahby A, Ramos-Fernández JM, Martínez-Escandell M, Sepúlveda-Escribano A, Silvestre-Albero J, Rodríguez-Reinoso F (2010) High surface area carbon molecular sieves for selective CO_2 adsorption. ChemSusChem 3:974–981. doi:10.1002/cssc.201000083

31. Mcdonald TM, Lee WR, Mason JA, Wiers BM, Hong CS, Long JR (2012) Capture of carbon dioxide from air and flue gas in the alkylamine-appended metal–organic framework mmen-Mg2(dobpdc). J Am Chem Soc 134:7056–7065. doi:10.1021/ja300034j

32. Drage TC, Blackman JM, Pevida C, Snape CE (2009) Evaluation of activated carbon adsorbents for CO_2 capture in gasification. Energy Fuel 23:2790–2796. doi:10.1021/ef8010614

33. Sharma A, Kumar S, Tripathi B, Singh M, Vijay Y (2009) Aligned CNT/polymer nanocomposite membranes for hydrogen separation. Int J Hydrog Energy 34:3977–3982. doi:10.1016/j.ijhydene.2009.02.068

34. Sharma A, Tripathi B, Vijay Y (2010) Dramatic improvement in properties of magnetically aligned CNT/polymer nanocomposites. J Membr Sci 361:89–95. doi:10.1016/j.memsci.2010.06.005

35. Su F, Lu C, Chung A-J, Liao C-H (2014) CO_2 capture with amine-loaded carbon nanotubes via a dual-column temperature/vacuum swing adsorption. Appl Energy 113:706–712. doi:10.1016/j.apenergy.2013.08.001

36. Zhao D, Ren J, Wang Y, Qiu Y, Li H, Hua K, Li X, Ji J, Deng M (2017) High CO_2 separation performance of Pebax®/CNTs/GTA mixed matrix membranes. J Membr Sci 521:104–113. doi:10.1016/j.memsci.2016.08.061

37. Razavi SS, Hashemianzadeh SM, Karimi H (2011) Modeling the adsorptive selectivity of carbon nanotubes for effective separation of CO_2/N_2 mixtures. J Mol Model 17:1163–1172. doi:10.1007/s00894-010-0810-9

38. Goh K, Setiawan L, Wei L, Jiang W, Wang R, Chen Y (2013) Fabrication of novel functionalized multi-walled carbon nanotube immobilized hollow fiber membranes for enhanced performance in forward osmosis process. J Membr Sci 446:244–254. doi:10.1016/j.memsci.2013.06.022

39. Park CH, Tocci E, Fontananova E, Bahattab MA, Aljlil SA, Drioli E (2016) Mixed matrix membranes containing functionalized multiwalled carbon nanotubes: Mesoscale simulation and experimental approach for optimizing dispersion. J Membr Sci 514:195–209. doi:10.1016/j.memsci.2016.04.011

40. Aroon MA, Ismail AF, Montazer-Rahmati MM, Matsuura T (2010) Effect of chitosan as a functionalization agent on the performance and separation properties of polyimide/multi-walled carbon nanotubes mixed matrix flat sheet membranes. J Membr Sci 364:309–317. doi:10.1016/j.memsci.2010.08.023

41. Fefey EG, Mohan R, Kelkar A (2011) Computational study of the effect of carbon vacancy defects on the Young's modulus of (6, 6) single wall carbon nanotube. Mater Sci Eng B 176:693–700. doi:10.1016/j.mseb.2011.02.019

42. Ge L, Zhu Z, Rudolph V (2011) Enhanced gas permeability by fabricating functionalized multi-walled carbon nanotubes and polyethersulfone nanocomposite membrane. Sep Purif Technol 78:76–82. doi:10.1016/j.seppur.2011.01.024

43. Logakis E, Pandis C, Peoglos V, Pissis P, Pionteck J, Pötschke P, Mičušík M, Omastova M (2009) Electrical/dielectric properties and conduction mechanism in melt processed polyamide/multi-walled carbon nanotubes composites. Polymer 50:5103–5111. doi:10.1016/j.polymer.2009.08.038

44. Xiong J, Zheng Z, Qin X, Li M, Li H, Wang X (2006) The thermal and mechanical properties of a polyurethane/multi-walled carbon nanotube composite. Carbon 44:2701–2707. doi:10.1016/j.carbon.2006.04.005

45. Zhang L, Wan C, Zhang Y (2009) Morphology and electrical properties of polyamide 6/polypropylene/multi-walled carbon nanotubes composites. Compos Sci Technol 69, 2212:–2217. doi:10.1016/j.compscitech.2009.06.005

46. Wang M, Wang Z, Li N, Liao J, Zhao S, Wang J, Wang S (2015) Relationship between polymer–filler interfaces in separation layers and gas transport properties of mixed matrix composite membranes. J Membr Sci 495:252–268. doi:10.1016/j.memsci.2015.08.019

47. Tatar A, Barati-Harooni A, Najafi-Marghmaleki A, Mohebbi A, Ghiasi MM, Mohammadi AH, Hajinezhad A (2016) Comparison of two soft computing approaches for predicting CO2 solubility in aqueous solution of piperazine. Int J Greenh Gas Control 53:85–97. doi:10.1016/j.ijggc.2016.07.037

48. http://Accelrys.Com/Products/Collaborative-Science/Biovia-Materials-Studio

49. Chen C, Wan J, Li W, Song Y (2015) Water contact angles on quartz surfaces under supercritical CO2 sequestration conditions: Experimental and molecular dynamics simulation studies. Int J Greenh Gas Control 42:655–665. doi:10.1016/j.ijggc.2015.09.019

50. Amani M, Amjad-Iranagh S, Golzar K, Sadeghi GMM, Modarress H (2014) Study of nanostructure characterizations and gas separation properties of poly(urethane–urea)s membranes by molecular

51. Amjad-Iranagh S, Golzar K, Modarress H (2014) Molecular simulation study of PAMAM dendrimer composite membranes. J Mol Model 20:1–20. doi:10.1007/s00894-014-2119-6

52. Azizi M, Mousavi SA (2015) CO_2/H_2 separation using a highly permeable polyurethane membrane: molecular dynamics simulation. J Mol Struct 1100:401–414. doi:10.1016/j.molstruc.2015.07.029

53. Fotoohi F, Amjad-Iranagh S, Golzar K, Modarress H (2015) Predicting pure and binary gas adsorption on activated carbon with two-dimensional cubic equations of state (2-D EOSs) and artificial neural network (ANN) method. Phys Chem Liq 1–22. doi: 10.1080/00319104.2015.1084877

54. Golzar K, Modarress H, Amjad-Iranagh S (2017) Separation of gases by using pristine, composite and nanocomposite polymeric membranes: a molecular dynamics simulation study. J Membr Sci 539:238–256. doi:10.1016/j.memsci.2017.06.010

55. Madkour TM, Mark JE (2013) Molecular modeling investigation of the fundamental structural parameters of polymers of intrinsic microporosity for the design of tailor-made ultra-permeable and highly selective gas separation membranes. J Membr Sci 431:37–46. doi:10.1016/j.memsci.2012.12.033

56. Sepehri A, Amjad-Iranagh S, Golzar K, Modarress H (2013) Homogeneous and heterogeneous nucleation of water vapor: a comparison using molecular dynamics simulation. Chem Phys 423:135–141. doi:10.1016/j.chemphys.2013.07.005

57. Yang L, Tong L, He X, Wagner HD, Wang R (2014) Molecular dynamic simulation of oblique pullout of carbon nanotube from resin. Comput Mater Sci 83:504–512. doi:10.1016/j.commatsci.2013.11.006

58. Khan MM, Bengtson G, Shishatskiy S, Gacal BN, Rahman MM, Neumann S, Filiz V, Abetz V (2013) Cross-linking of polymer of intrinsic microporosity (PIM-1) via nitrene reaction and its effect on gas transport property. Eur Polym J 49:4157–4166. doi:10.1016/j.eurpolymj.2013.09.022

59. Moosavi F, Abdollahi F, Razmkhah M (2015) Carbon dioxide in monoethanolamine: Interaction and its effect on structural and dynamic properties by molecular dynamics simulation. Int J Greenh Gas Control 37:158–169. doi:10.1016/j.ijggc.2015.03.015

60. Tian Z, Wang S, Wang Y, Ma X, Cao K, Peng D, Wu X, Wu H, Jiang Z (2016) Enhanced gas separation performance of mixed matrix membranes from graphitic carbon nitride nanosheets and polymers of intrinsic microporosity. J Membr Sci 514:15–24. doi:10.1016/j.memsci.2016.04.019

61. Boyd PG, Moosavi SM, Witman M, Smit B (2017) Force-field prediction of materials properties in metal-organic frameworks. J Phys Chem Lett 8:357–363. doi:10.1021/acs.jpclett.6b02532

62. Mercado R, Vlaisavljevich B, Lin L-C, Lee K, Lee Y, Mason JA, Xiao DJ, Gonzalez MI, Kapelewski MT, Neaton JB, Smit B (2016) Force field development from periodic density functional theory calculations for gas separation applications using metal–organic frameworks. J Phys Chem C 120:12590–12604. doi:10.1021/acs.jpcc.6b03393

63. Hölck O, Böhning M, Heuchel M, Siegert MR, Hofmann D (2013) Gas sorption isotherms in swelling glassy polymers-detailed atomistic simulations. J Membr Sci 428:523–532. doi:10.1016/j.memsci.2012.10.023

64. Staiger CL, Pas SJ, Hill AJ, Cornelius CJ (2008) Gas separation, free volume distribution, and physical aging of a highly microporous spirobisindane polymer. Chem Mater 20:2606–2608. doi:10.1021/cm071722t

65. Li P, Chung T, Paul D (2013) Gas sorption and permeation in PIM-1. J Membr Sci 432:50–57. doi:10.1016/j.memsci.2013.01.009

66. Li P, Chung T, Paul D (2014) Temperature dependence of gas sorption and permeation in PIM-1. J Membr Sci 450:380–388. doi:10.1016/j.memsci.2013.09.030

dynamics simulation. J Membr Sci 462:28–41. doi:10.1016/j.memsci.2014.03.018

67. Quan S, Li SW, Xiao YC, Shao L (2017) CO$_2$-selective mixed matrix membranes (MMMs) containing graphene oxide (GO) for enhancing sustainable CO$_2$ capture. Int J Greenh Gas Control 56: 22–29. doi:10.1016/j.ijggc.2016.11.010

68. Rezaei M, Ismail AF, Hashemifard SA, Bakeri G, Matsuura T (2014) Experimental study on the performance and long-term stability of PVDF/montmorillonite hollow fiber mixed matrix membranes for CO$_2$ separation process. Int J Greenh Gas Control 26: 147–157. doi:10.1016/j.ijggc.2014.04.021

69. Kim HJ, Kim D-G, Lee K, Baek Y, Yoo Y, Kim YS, Kim BG, Lee J-C (2016) A carbonaceous membrane based on a polymer of intrinsic microporosity (PIM-1) for water treatment. Sci Rep 6:1–8. doi:10.1038/srep36078

70. Lanč M, Pilnáček K, Vopička O, Friess K, Bernardo P, Bazzarelli F, Tasselli F, Clarizia G, Mason C, Maynard-Atem L (2016) Effect of physical aging on the gas transport and sorption in PIM-1 membranes. Polymer doi:10.1016/j.polymer.2016.10.040

71. Liu L, Nicholson D, Bhatia SK (2015) Impact of H$_2$O on CO$_2$ separation from natural gas: Comparison of carbon nanotubes and disordered carbon. J Phys Chem C 119:407–419. doi:10.1021/jp5099987

72. Liu Z, Liu C, Li L, Qin W, Xu A (2016) CO$_2$ separation by supported ionic liquid membranes and prediction of separation performance. Int J Greenh Gas Control 53:79–84. doi:10.1016/j.ijggc.2016.07.041

73. Mondal A, Barooah M, Mandal B (2015) Effect of single and blended amine carriers on CO$_2$ separation from CO$_2$/N$_2$ mixtures using crosslinked thin-film poly(vinyl alcohol) composite membrane. Int J Greenh Gas Control 39:27–38. doi:10.1016/j.ijggc.2015.05.002

74. Saeed M, Deng L (2016) Carbon nanotube enhanced PVA-mimic enzyme membrane for post-combustion CO$_2$ capture. Int J Greenh Gas Control 53:254–262. doi:10.1016/j.ijggc.2016.08.017